UNIVERSITY OF COPENHAGEN
FACULTY OF SCIENCE

Master's Thesis

Readout and Control of Semiconductor-Nanowire-Based Superconducting Qubits

Author:
Anders Kringhøj

Supervisor:
Karl D. Petersson

July 14, 2016

Center for Quantum Devices

Abstract

Superconducting quantum bits (qubits) are promising candidates for scalable, fault-tolerant quantum computation. Being able to determine a quantum state with a single measurement is essential for using any quantum system for computation. In this thesis single shot readout is implemented for hybrid semiconductor based superconducting qubits by integrating a near quantum limited parametric amplifier into the existing cryogenic setup. We achieve a readout fidelity of around 70%, limited by the $\sim$ 1-2 μs lifetimes. However prolonging qubit coherence in future experiments will potentially allow the readout fidelity to reach the state of the art. Combining the single shot readout with two-qubit operations the first steps towards entanglement demonstration are taken. Further experiments implementing feedback to correct drift in qubit frequency along with an extensive study of qubit anharmonicity are performed to investigate the physics of the qubit.

Acknowledgements

During my thesis work at the Center for Quantum devices I have had many memorable and learning experiences, which I am grateful of. Through my time as a Master's student I have had the pleasure of working with some great people, whom I would like to thank. Firstly I would like to thank Charles Marcus for letting me into the laboratory and allowing me to explore what it means to be an experimentalist in all its aspects.
I would like to thank my supervisor Karl Petersson for very competent guidance and for taking interest in my learning.
Next I would like to thank my two go-to-guys, Thorvald Larsen and Lucas Casparis. A big thank you to Thorvald for taking me under his wings, when I started and for always being willing to help me with whatever questions I have had ranging from fabrication details to measurement techniques. Also a big thank you to Lucas for teaching and explaining me many experimental details and tricks and for support in all the experiments, I have been involved in.
I also want to thank Laurits Andersen for supporting me with the fridge setup and helping with the measurements and improvements performed on the two-qubit device.
Next I would like to express my gratitude to the one and only Shiv (Shivendra Upadhyay) for always being willing to help me out with any kind of fabrication or tool issues I may have encountered at any time of the day and week.
Many other people not mentioned have helped me and contributed to making my time at Qdev enjoyable. So thank you to everyone in Qdev!

Contents

Chapter 1

Introduction

1.1 Quantum computing

Manipulating and controlling information in a system governed by the laws of quantum mechanics is an intriguing idea studied in the field of quantum information processing. Classical computing builds on classical bits, which can take digital values of either 0 or 1. In quantum computing two level quantum mechanical systems form quantum bits (qubits). Qubits are described by a state vector, $|\Psi\rangle$, which can be any superposition of the two qubit eigenstates $|0\rangle$ and $|1\rangle$, $|\Psi\rangle = a\,|0\rangle + b\,|1\rangle$, where a and b are the state amplitudes that can take any complex values within $|a|^2 + |b|^2 = 1$. This probabilistic nature of quantum mechanics is the fundamental ground stone for quantum computing. If two such qubits are entangled the general state vector is a superposition of the four different two qubit states, $a\,|00\rangle + b\,|01\rangle + c\,|10\rangle + d\,|11\rangle$. This means that to fully understand the system four probability amplitudes need to be known. This is in contrary to a classical two-bit system, where one needs two numbers to understand the system. Since n entangled qubits are described by a 2^n-dimensional state vector, the dimension of state vector grows exponentially with the number of entangled qubits as opposed to the classical system, where the complexity grows linearly with the number of classical bits. A quantum processor can potentially run algorithms exponentially faster than a classical processor and therefore solve problems impossible to compute on a classical computer. Examples of applications for a quantum processor are Shor's algorithm for prime factorisation [1] or simulation of chemical reactions [2] among many others.

Experimentally it is a huge challenge to make a robust qubit system as quantum errors will occur due to imperfect operations or loss of coherence because of environmental couplings. Therefore a big field of study is fault-tolerant quantum computing, where logical qubits are encoded into several physical qubits. In such code schemes fault-tolerant qubits can be realised to achieve scalable and stable qubit systems [1].

1.2 Experimental realisation

There are tremendous challenges in experimentally building such a controllable quantum system, as described by the famous DiVincenzo criteria [3]:

- "A scalable physical system with well characterized qubits"
- "The ability to initialize the state of the qubits to a simple fiducial state, such as $|000...\rangle$"
- "Long relevant decoherence times, much longer than the gate operation time"
- "A "universal" set of quantum gates"
- "A qubit-specific measurement capability"

Throughout the relatively short lifetime of this field many different coherent two-level systems have been explored as candidates for building a scalable and controllable qubit system. Examples of qubit systems are ion traps, where the two-level qubit system consists of the spin states of atomic ions confined in an electromagnetic field [4], or spin qubits, where confined electronic spin states act as the qubit system [5]. Development of topological protected systems such as Majorana fermions is also an area of great interest [6]. All candidates show strengths and weaknesses, for instance, ion traps are very coherent systems with long lifetimes but manipulation of qubit states is troublesome and slow.

The qubit type of investigation in this thesis are superconducting qubits, which have shown to be a strong candidate of fulfilling the DiVincenzo criteria. Superconducting qubits embedded in a circuit quantum electrodynamics (cQED) architecture allow control, manipulation and state readout of these systems through well known microwave techniques. Multi qubit system of up to nine qubits have demonstrated single qubit gate fidelities exceeding 0.99 and coherence times reaching several tens of μs, which make prospects of scaling these systems very promising [7].

In particular a promising candidate with highly coherent qubit states is the transmon qubit. As with all superconducting qubits the transmons rely on the Josephson junction as its non-linear element, which makes it possible to address the two lowest levels individually. Currently leading groups in the community construct their junctions from an insulating tunnel junction either in a SQUID loop that allows tuning of qubit frequencies via magnetic fluxes [7] or in a simpler configuration in which tuning the qubit frequencies is impossible [8]. Both ways have some disadvantages as scaling a system without tuneability will be difficult due to variations in fabrication. On the other hand tuning the qubits with magnetic fluxes requires mA-level dissipative currents to flow in the mK cryogenic environment of the experiments, which might potentially lead to heating and decoherence.

This thesis project investigates a new kind of hybrid semiconductor based superconducting qubit called the gatemon, where the Josephson junction element is a semiconductor sandwiched between the superconducting electrodes, constructed using superconductor-semiconductor nanowires [9, 10]. This semiconducting junction allows the qubits to be tuned by low dissipative gate voltages. The early demonstrations of these qubit systems take advantage of the same readout and control mechanism as conventional transmons and it is believed that the coherence of the gatemon is not limited by this change of junction element type [11].

1.3 Outline

The aim of this thesis project is to implement single shot readout, single line qubit control and feedback based stabilisation of the gatemon qubit frequency. Additionally experiments towards demonstration of two qubit entanglement are performed. This thesis introduces some of the theoretical concepts of transmon qubits in Chapter 2. In particular the theory of the qubit operated in the dispersive regime relevant for the qubit measurements is presented. Chapter 3 gives an overview of the device fabrication, the measurement setup and experimental techniques. In Chapter 4 measurements of a two qubit device are presented and analysed. The main conclusions of this thesis work are presented in Chapter 5 along with the future prospects for gatemon qubits.

Chapter 2

Theory

In this Chapter the basic concepts of transmon and gatemon qubits are explained. It will start out considering the simple circuit of an inductor and a capacitor, an LC-circuit. From here the fundamentals of transmon qubits are explained followed by a description of how to implement superconducting qubits in a circuit quantum electrodynamics architecture allowing qubit control and readout.

2.1 LC oscillators to transmon qubits

As superconducting qubits are constructed of quantised circuits a natural starting point is to consider the LC-circuit, see circuit diagram in Fig. 2.1(a). The LC-circuit consists of two non-dissipative elements. In the lumped-element approximation the system is described by two parameters, the capacitance, C, of the capacitor and the inductance, L, of the inductor [12]. A capacitive energy is associated with this system of $\frac{Q^2}{2C}$, understood as the energy that can be stored in the capacitor, where Q is the magnitude of the charge on each capacitor plate. There is also an inductive energy associated with the system of $\frac{\Phi^2}{2L}$, where Φ is the flux through the inductor created by the current flow.

Since Φ and Q are canonically conjugate variables the Hamiltonian can be written,

$$\hat{H} = \frac{\hat{\Phi}^2}{2L} + \frac{\hat{Q}^2}{2C} \tag{2.1}$$

by quantising Φ and Q [12]. This Hamiltonian is that of a harmonic oscillator and the LC-circuit can therefore be identified as a quantised harmonic oscillator. This means that the LC-circuit gives rise to discrete energy levels spaced evenly by $\hbar\omega$, where $\omega = 1/\sqrt{LC}$. An LC-oscillator cannot be used as a qubit as the energy level spacing is harmonic and the two lowest levels can therefore not be addressed individually. In order to create an addressable two-level system non-linearity is required.

The Josephson junction (JJ) provides both a non-linear and non-dissipative element. Exchanging the inductor with a JJ in the LC-circuit will lead to a non-linear Hamiltonian, which can provide the

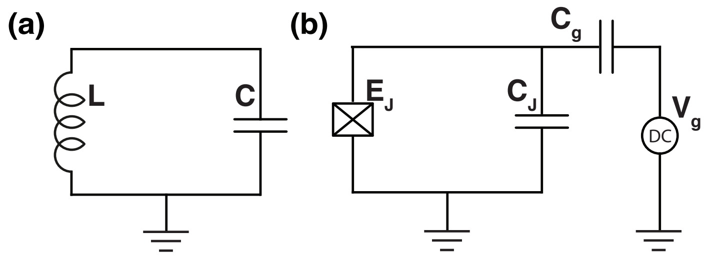

Figure 2.1: (a) Simple circuit diagram of an LC-oscillator. (b) Simple circuit diagram of CPB-qubit. The qubit consists of a JJ with an associated energy, E_J, and a total capacitance, $C = C_J + C_g$. The charge on the qubit island is controlled with a DC voltage, V_g, which is coupled to the qubit island via a capacitance C_g.

desired anharmonic energy levels needed to create a qubit system. Connecting two superconductors with a weak link of a non-superconducting region allows the superconducting state to persist across the junction. A weak link is understood as $L \ll \xi$, where L is the length of the junction and ξ is the coherence length of the weak link. From Ginzburg-Landau theory, ξ can be understood as the length scale with which the superconducting state decay into the normal state [13]. As the superconducting state can survive across the junction the only degree of freedom between the two superconductors is the phase difference, ϕ, of their wave functions since both superconductors will be in their ground state, namely the superconducting condensate.

Remarkably ϕ gives rise to a current even with no external voltage drop known as the DC Josephson effect,

$$I = I_c \sin(\phi), \tag{2.2}$$

where I_c is the critical current of the junction, i.e. the largest supercurrent that can run across the junction.

A constant voltage drop, V, across the junction gives rises to a time varying phase, known as the AC Josephson effect,

$$V = \frac{\hbar}{2e}\frac{\partial\phi}{\partial t} = \frac{\Phi_0}{2\pi}\frac{\partial\phi}{\partial t}, \tag{2.3}$$

where $\Phi_0 = \frac{h}{2e}$ is the flux quantum. Combining these two effects the time derivative of the current can be found,

$$\frac{dI}{dt} = I_c \cos(\phi)\frac{\partial\phi}{\partial t} = \frac{2\pi V I_c \cos(\phi)}{\Phi_0}. \tag{2.4}$$

This relation is of the same form as the voltage induced across an inductor, $V = -L\frac{dI}{dt}$ and therefore a JJ is typically described as a non-linear inductor with inductance, L_J,

$$L_J = \frac{\Phi_0}{2\pi I_c \cos(\phi)}. \tag{2.5}$$

In general all superconducting qubit types are based on a quantised circuit involving a JJ. These qubit circuits can be divided into three base types of qubits depending on the sensitive parameter of the system: Cooper pair box (CPB), flux and phase qubit [14].

As the transmon qubit has the most resemblance to the CPB qubit it is instructive to consider it first. The CPB is constructed as shown in Fig. 2.1(b). As with the LC oscillator a charging energy, $E_C = \frac{e^2}{2C}$, is associated with the capacitance of the system. Here $C = C_g + C_J$ is the total capacitance of the system with contribution from the gate capacitance, C_g, and the junction capacitance, C_J. With the presence of the JJ only an integer number of Cooper pairs can tunnel across the junction giving rise to a factor of $(2e)^2$ in the energy term. The potential energy term associated with storing Cooper pairs on the capacitor is therefore, $U_C = 4E_C(\hat{n} - n_g)^2$, where $\hat{n}$ is the number of Cooper pairs tunnelled across the junction and $n_g = \frac{-C_g V_g}{2e}$ is an offset charge controlled with a voltage bias, V_g.

There is also an energy associated with the JJ, which is due to the phase difference across the junction. By considering the DC and the AC Josephson effects the energy of a current driven JJ can be found to be,

$$\int_0^t IV\,dt = \int_0^t I_c \sin(\phi) \frac{\Phi_0}{2\pi} \frac{\partial \phi}{\partial t} dt = \int_0^\phi I_c \sin(\phi') \frac{\Phi_0}{2\pi} d\phi' = \frac{\Phi_0 I_c}{2\pi}(1 - \cos(\phi)) = E_J(1 - \cos(\phi)). \tag{2.6}$$

With $E_J = \frac{\Phi_0 I_c}{2\pi}$ being the characteristic Josephson energy associated with Cooper pairs tunnelling across the junction.

Collecting the energy terms therefore gives rise to the Hamiltonian,

$$\hat{H} = 4E_C(\hat{n} - n_g)^2 - E_J \cos\left(\hat{\phi}\right). \tag{2.7}$$

The solution of this Hamiltonian, which is explained in great details in e.g. Refs. [15, 16], is periodic in the number of Cooper pairs, see Fig. 2.2(a). With this charge dispersion it is clear that the CPB qubit is susceptible to charge noise. Even though coherence is improved by operating at first order insensitive sweet spots, the CPB is not a satisfactory candidate for a scalable qubit system as operating and coupling multiple qubits will require leaving these sweet spots. Instead it was found that increasing $\frac{E_J}{E_C}$ by adding a shunt capacitance to the circuit will exponentially suppress the sensitivity to charge fluctuations, see Figs. 2.2(a)-(d). With charge on the qubit no longer being well defined the separate voltage control of n_g is not needed for the transmon qubit.

Increasing $\frac{E_J}{E_C}$ will lead to a decrease in the anharmonicity, $\alpha = E_{12} - E_{01}$, E_{ij} being the qubit transition energies. Anharmonicity is crucially needed for a qubit system to be controllable and luckily α only decreases asymptotically to zero in a algebraic power law for large $\frac{E_J}{E_C}$ [15]. Therefore in the regime of $\frac{E_J}{E_C} \gg 1$, called the transmon regime, charge noise sensitivity is strongly suppressed and a level of anharmonicity allowing fast qubit control is maintained. However a compromise is that α is not only lowered, but it also turns negative in this regime as opposed to a CPB operated at $n_g \approx 1/2$. Therefore when operating in the transmon regime the system is more susceptible to leakage into higher, non-computational states. In the transmon approximation $\alpha \approx -E_C$ and as

α sets a bound on how fast qubit states can be manipulated a good comprise for $\frac{E_J}{E_C}$ needs to be achieved. For ratios of $\frac{E_J}{E_C} \sim 50 - 100$ the systems are essentially insensitive to charge fluctuations and the anharmonicity is still large enough for qubit operations, which are a few ns long [15].

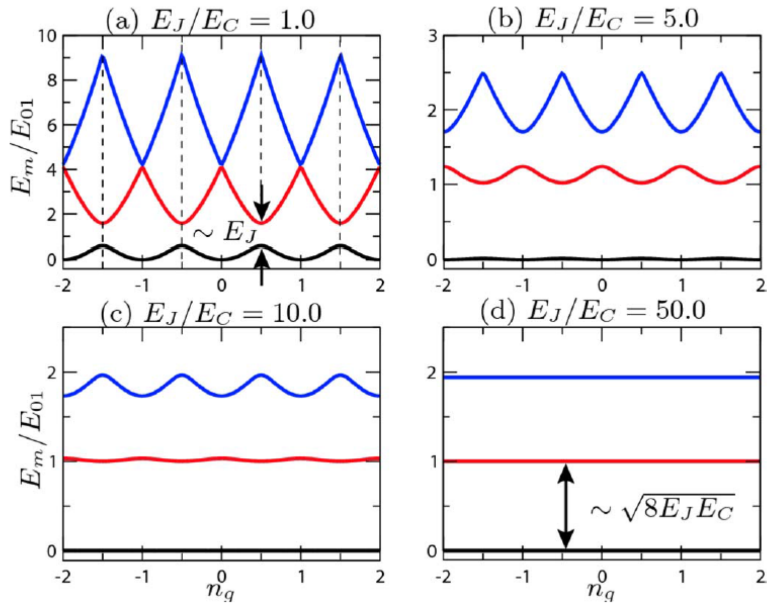

Figure 2.2: Numerical solutions of the CPB-Hamiltonian solved in four different $\frac{E_J}{E_C}$ regimes as a function of the offset charge, n_g. It is observed how the charge dependence is strongly reduced in the $\frac{E_J}{E_C} \gg 1$ regime. The energy scale on the y-axis is given in terms of the transition energy from $|0\rangle \rightarrow |1\rangle$ at the sweet spot, i.e. $n_g = 1/2$. Figure from [15].

2.2 cQED

Cavity quantum electrodynamics (cavity QED) describes systems of atoms coupled to photon modes. The concepts of cavity QED have been adapted to superconducting circuits, where superconducting qubits acting as artificial atoms are coupled to electromagnetic modes of transmission line microwave resonators in an architecture called circuit QED (cQED). These systems have shown to be very promising as control and readout are achieved relatively easy via microwave signals. Additionally internal losses of these systems can be very low potentially allowing long lifetimes of the qubit systems [17]. A circuit with a superconducting qubit coupled to a resonator (see Fig. 2.3) can be described by the so called Jaynes-Cummings Hamiltonian, which treats the anharmonic qubit oscillator as a two level spin 1/2 system:

$$\hat{H} = \hbar\omega_r(\hat{a}^\dagger\hat{a} + \frac{1}{2}) + \frac{\hbar\omega_{01}}{2}\hat{\sigma}_z + \hbar g(\hat{a}^\dagger\hat{\sigma}_- + \hat{a}\hat{\sigma}_+). \tag{2.8}$$

The first term of $\hat{H}$ describes the harmonic oscillator of the resonator, where ω_r is the cavity resonance frequency, $\hat{a}^\dagger$ and $\hat{a}$ are the harmonic creation and annihilation operators. The second term

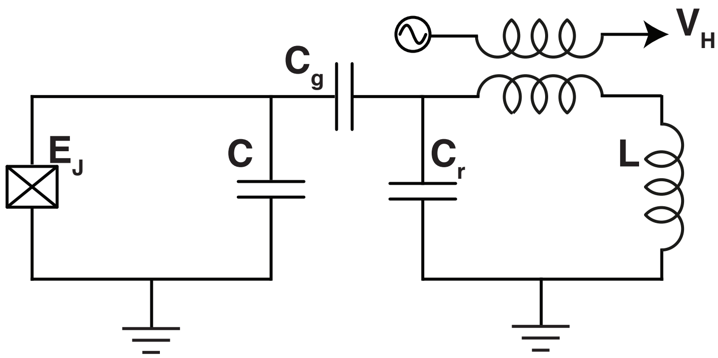

Figure 2.3: Circuit diagram of a gatemon qubit coupled via a capacitance, C_g, to a transmission line resonator described as an LC-oscillator. The qubit is represented in the same way as the CPB-qubit, but the total capacitance, C, takes contribution from both the small junction capacitance and the big shunt capacitance. The LC-resonator is inductively coupled to a transmission line. By measuring the transmission, V_H, through this transmission line the resonance frequency and hereby qubit state can be probed.

describes the two level qubit system, where ω_{01} is the qubit transition frequency, $\hat{\sigma_z}$ is the spin 1/2 Pauli Z operator. Finally the third term describes the qubit-cavity interaction, where g is the qubit-cavity coupling and $\sigma_\pm$ are the raising and lowering operators of the spin system, where the $\hat{a}^\dagger\hat{\sigma}_-$ and $\hat{a}\hat{\sigma}_+$ terms can be understood as exchange of an excitation from the qubit to the resonator and from the resonator to the qubit respectively. Detailed derivations and descriptions of cQED and the Jaynes-Cummings Hamiltonian are given in Refs. [15, 17, 18].

Experiments in this thesis are performed in the dispersive limit, where $g \ll |\omega_{01} - \omega_r|$. In this limit $\hat{H}$ can be approximated by,

$$\hat{H}_{\text{eff}} = \frac{\hbar\omega'_{01}}{2}\hat{\sigma}_z + (\hbar\omega'_r + \hbar\chi\hat{\sigma}_z)\hat{a}^\dagger\hat{a}, \tag{2.9}$$

where $\chi = \chi_{01} - \chi_{12}/2$, $\omega'_r = \omega_r - \chi_{12}$ and $\omega'_{01} = \omega_{01} + \chi_{01}$ and $\chi_{ij} = \frac{g_{ij}^2}{\omega_{ij}-\omega_r}$. This way the bare qubit and resonance frequencies have been renormalised due to the interaction. The main point from this Hamiltonian is that ω'_r will shift by $\pm\chi$ depending on the qubit state as seen from the second term, $(\hbar\omega'_r + \hbar\chi\hat{\sigma}_z)\hat{a}^\dagger\hat{a}$. In this way cQED offer simple read out of qubit states based on transmission measurements probing the cavity resonance frequency.

To operate a transmon in the dispersive limit the right regime of g, Δ, qubit decay rate, γ and the resonator decay rate, κ needs to be satisfied. $g \ll |\omega_{01} - \omega_r|$ is not the only requirement as $2\chi > \kappa$ is needed to be able to resolve the qubit state dependent pull on ω'_r. Also $g > \gamma, \kappa$ is a requirement as the coupling need to be sufficiently large to measure faster than the decay of the qubit and resonator. However in cavity QED the spontaneous emission rate, γ_κ, of an atom is increased when it couples to a cavity. This effect is known as the Purcell effect [19]. Similarly coupling a transmon to a transmission line resonator gives rise to the same effect with $\gamma_\kappa = \frac{g^2}{\Delta^2}\kappa$. Potentially γ_κ can be the limiting contribution to coherence of the qubit system and it is therefore important to find a compromise between the various parameters. Obviously if κ is lowered γ_κ will be reduced. On the other hand a small κ will make readout slow because the characteristic time scale for photons to enter or leave the cavity is $1/\kappa$. In this experiment $g \approx 100$ MHz, $Q \approx 10^4$, $\omega_r/2\pi \sim$ 7-8 GHz and $\Delta \sim$ 2-4 GHz allow fast readout in the dispersive regime without being Purcell limited.

2.2.1 Qubit rotations

Due to the quantum mechanical behaviour of qubit states, where the state can take any superposition of the eigenstates, single qubit states are typically described as a vector in a sphere called the Bloch sphere. In this representation, the two ends of the z-axis correspond to the qubit eigenstates $|0\rangle$ and $|1\rangle$ as labelled in Fig. 2.4. Any rotation can then be described by the angle of rotation and the axis around which the state vector is rotated. For instance a pulse that brings the qubit vector onto the Bloch equator is referred to as a $\pi/2$ pulse usually around either the x-axis or the y-axis. Even though it is only the z-component that can be measured in a transmon measurement the entire qubit vector can be mapped out by projecting the x- or y-component onto the z-axis with $\pi/2$ pulses. The dispersive Jaynes-Cummings Hamiltonian does not provide the full understanding

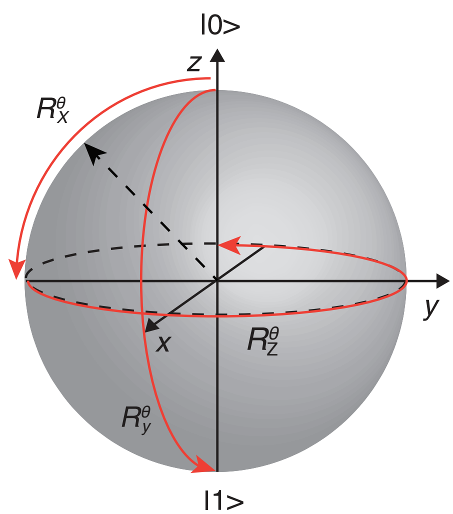

Figure 2.4: Bloch sphere representing the qubit state vector. Rotations around the three axes are labelled with a red arrow. R_i^θ refers to the angle θ the vector is rotated around an axis i. The dashed arrow illustrates the qubit state vector, $|\psi\rangle$, which can take any orientation in the sphere corresponding to any superposition of $|0\rangle$ and $|1\rangle$.

of such rotations in a transmon qubit. These rotations are induced by the external microwave drive and the coupling of the microwave drive used to manipulate the qubits will naturally affect the Hamiltonian. This drive effect is conveniently explained in the rotating frame of the microwave drive frequency, ω_d. In the rotating frame this drive gives rise to an additional term, which is explained in details in Refs [12, 16]. Still treating the transmon as a pure two level system in the dispersive limit, the Hamiltonian becomes,

$$\hat{H} = (\hbar\Delta_r + \hbar\chi\hat{\sigma}_z)\hat{a}^\dagger\hat{a} + \frac{\hbar\Delta_d}{2}\hat{\sigma}_z + \frac{\hbar}{2}\left(\Omega_R^x(t)\hat{\sigma}_x - \Omega_R^y(t)\hat{\sigma}_y\right), \tag{2.10}$$

where $\Delta_r = \omega_r - \omega_d$, $\Delta_d = \omega_{01} - \omega_d$. $\Omega_R^x(t)$ and $\Omega_R^y(t)$ are the two Rabi drive amplitudes $\pi/2$ out of phase with each other. The last two spin terms of this Hamiltonian closely resembles that of a spin in a static magnetic field with an applied perpendicular oscillating field [20]. From the $\frac{\hbar\Delta_d}{2}\hat{\sigma}_z$ term it is seen that $\Delta_d \neq 0$ will induce rotations around the z-axis with oscillation frequency Δ_d. Also the $\frac{\hbar}{2}\left(\Omega_R^x(t)\hat{\sigma}_x - \Omega_R^y(t)\hat{\sigma}_y\right)$ terms reveals that rotations around the x- and y-axis can be controlled by choosing the phase of the drive signal, where the frequency of the rotations is controlled by the amplitude and width of the signal. Note that rotations in the Bloch sphere are also in the rotating frame of the drive frequency. These rotations will be experimentally explored in Section 4.1.2.

2.2.2 Qubit-qubit coupling

Coupling qubits together is an essential part of any qubit system. In cQED, two superconducting qubits can be coupled capacitively, giving rise to the coupling term, $\hat{H}_c$, in addition to Eq. 2.9,

$$\hat{H}_c = \hbar g_q \left(\hat{\sigma}_-^{(1)}\hat{\sigma}_+^{(2)} + \hat{\sigma}_-^{(2)}\hat{\sigma}_+^{(1)}\right), \tag{2.11}$$

where the qubit-qubit coupling, g_q, is given, $g_q = \frac{C_q\sqrt{f_{01}^{(1)}f_{01}^{(2)}}}{2\sqrt{C_\Sigma^{(1)}C_\Sigma^{(2)}}}$ [21]. The index indicates each qubit and C_q is the mutual capacitance between two qubits. Even though g is fixed, the qubit-qubit interaction will effectively be turned off when $g_q \ll |\omega_{01}^{(1)} - \omega_{01}^{(2)}|$ [21]. Therefore when two qubits are far detuned from each other the coupling is suppressed and the qubits can be considered as two individual systems.

Another interesting feature to observe from the coupling term is that it will give rise to exchange of excitations from one qubit to the other when the qubits are degenerate. If one of the qubits is prepared in $|0\rangle$ and then brought into resonance with the other qubit prepared in $|1\rangle$ the excitation will oscillate with $2g_q/2\pi$ between $|01\rangle$ and $|10\rangle$. This way of swapping a qubit excitation is investigated experimentally in Section 4.6.

2.3 Gatemon qubits

The development in the superconducting community has been such that almost all superconducting qubits are based on the tunnel junction, which is typically constructed by sandwiching an insulating oxide layer in between two superconducting aluminium layers. Developments in materials and interfaces have lead to high quality tunnel junctions. However the only way to tune the qubit frequency of these qubits based on tunnel junctions is to arrange two junctions in a loop. Threading the loop with magnetic flux allows tuning the phase difference between the superconductors, which tunes an effective E_J. As magnetic flux is generated by introducing dissipative currents this approach will potentially have difficulties scaling the electronics while still maintaining ultra low temperatures.

A different approach is to use a semiconductor as the weak link between the superconducting electrodes. Having a semiconductor junction allows tuning the carrier density, n, with a gate voltage, V_g. This way $E_J = \frac{\hbar I_c}{2e}$ can be tuned as $I_c \propto n$ in a JJ [13]. By introducing gateability the qubit system no longer requires flux control, but can instead be controlled using voltages on high impedance gate lines that draw negligible current. The realisation of a coherent semiconductor/superconductor qubit is based on molecular beam epitaxy (MBE) grown InAs/Al nanowires

[22]. These nanowires consist of an InAs core with an Al shell grown around the InAs wire. The epitaxially matched Al induces a superconducting gap in the semiconducting InAs. By etching away a ~ 200 nm region of the Al shell a JJ is created. Apart from the junction fabrication these gatemons are constructed in essentially the same way as traditional transmons. The first generations of gatemon qubit devices showed coherence times of ~ 1 μs [9] and the second generation showed further improvement [11] reaching a few μs. From these experiments the coherence of these qubits are believed to be limited by losses in the capacitor rather than in the junction [11]. One of the aims of future work is to achieve similar levels of coherence and control as for conventional transmons.

Chapter 3

Measurement setup and methods

While experimental data shown in this thesis are all from the same two-qubit device, see Figs. 3.1(a) and 3.1(b), all gatemon devices involve very similar fabrication and measurement techniques. In this Chapter I will therefore describe the standard fabrication techniques required to build a gatemon qubit device based on the process used to fabricate the two-qubit device. Hereafter the experimental setup and techniques for qubit measurements and manipulation are described using the two-qubit device as an example.

3.1 Device

The circuit for the two-qubit device is patterned on a Si substrate using standard UV and electron beam lithography (EBL) and electron beam metal evaporation [23]. The device substrate is first covered with a thin 100 nm aluminium film acting as a ground plane. From here the transmission line, control lines, and qubit islands are created by UV patterning resist and wet etching away aluminium strip lines. Hereafter nanowires are randomly deposited in EBL patterned windows and a $\sim$ 200nm segment of the Al shell is etched away acting as the Josephson element, see Fig. 3.1(c). At this point many nanowires have been etched, but to create a qubit only one nanowire is needed. To decide which nanowire to proceed with the nanowires are imaged with a scanning electron microscope (SEM). Hereafter Al control side gates and nanowire contacts are deposited using Kaufmann argon milling and metal evaporation, finishing the qubit circuit in a cQED architecture as shown in Fig. 3.2. A detailed description of device fabrication is found in Appendix A.

The designed distances and sizes of the various elements in the device are determined by electrostatic capacitance simulations. The sizes of the qubit islands correspond to $E_C = \frac{e^2}{2C_\Sigma} \approx 200$ MHz simulating the total capacitance C_Σ of the island. The qubit-cavity coupling, g, is determined by C_Σ, C_g (capacitance between qubit island and resonator.) and V^0_{rms}, which is the root-mean square vacuum voltage fluctuations [18]. From simulations of the previous gatemon design $g \sim 100$ MHz is estimated [9, 11]. This is chosen to be an appropriate value giving sufficient coupling to the readout resonator but low enough to operate in the dispersive regime and not to be limited by the Purcell effect as discussed in Section 2.2.

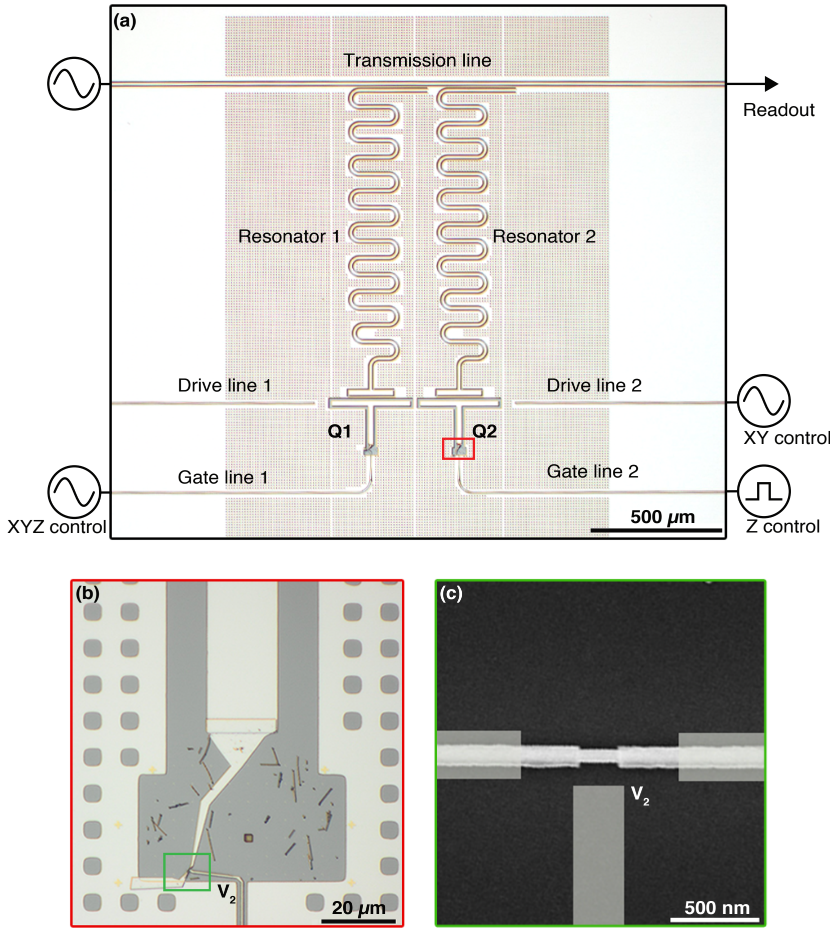

Figure 3.1: (a) Optical micrograph of the two qubit device. The device pattern is etched out on a Si-substrate covered with 100 nm evaporated Al. The transmission line, which is coupled to the resonators for qubit readout, is seen in the top of the image. The two resonators going down from the transmission line to the qubit island are designed to be identical except that resonator 1 is 27 μm longer than resonator 2. The T-shaped qubit islands are capacitively coupled to the resonators and connected to the nanowires via Al contacts. The connected nanowires are placed in the window at the bottom of the islands, as indicated by the red square for qubit 2 (Q2). The control lines are also identical for both qubits. Next to the qubit islands the drive lines are patterned and below the qubit islands the gate lines are defined. The microwave sources used for XY control as well as readout are labelled. Z controlled is achieved with DC pulses as labelled for Q2. For qubit 1 (Q1) DC pulses for Z control are combined with the XY control signals. (b) Micrograph of the nanowire region of Q2 labelled with a red square in (a). The Al strip line coming down from the top is the qubit island, which is contacted to the nanowire. The other side of the nanowire junction is contacted to the ground plane. In the bottom of the image the gate line is seen. (c) SEM-image of the nanowire placed in the green square in (b) with the design for the contacts and gate overlaid. The upper contact is connected to the qubit island and the lower contact is connected to ground.

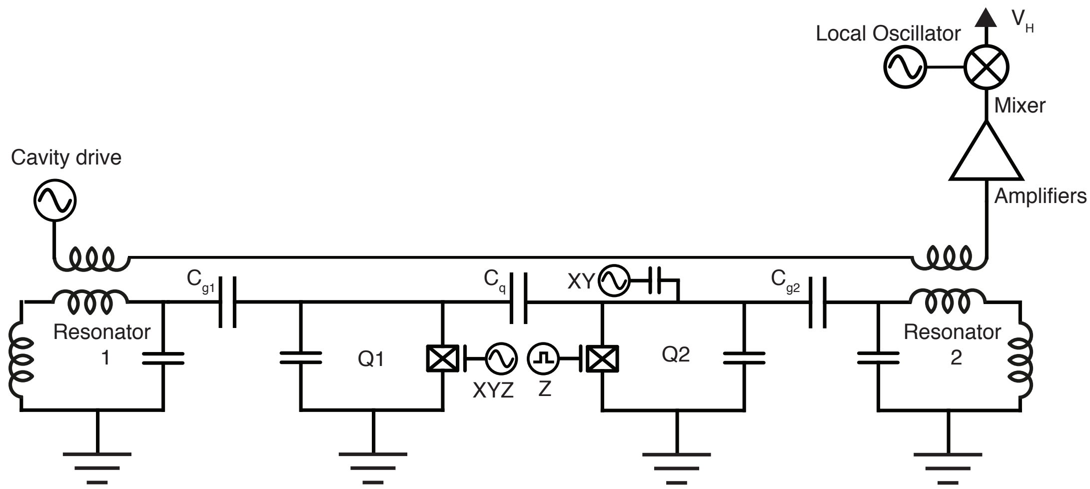

Figure 3.2: Circuit diagram of the two gatemon qubit device. The two qubits are coupled to each other via a capacitance, C_q. Each qubit is coupled to an LC-resonator as shown previously. Both resonators are inductively coupled to the transmission line. The transmission signal is mixed with a local oscillator before being read out by the data acquisition software. Note how Q1 is coupled to only one microwave source controlling all axes. Q2 is coupled to both a microwave source for XY-control and a DC source for controlling the z-axis.

3.2 Heterodyne readout

One of the big advantages of superconducting qubits is that control and manipulation are based on well developed microwave techniques. In particular, gatemon control around all axes in the Bloch sphere is achieved with voltage pulses, either microwave pulses for XY-control or DC for Z-control.

In Fig. 3.3 the measurement setup for the two qubit sample is shown. The experiments are carried out in a dilution refrigerator from Oxford instruments with the sample mounted in a < 50 mK environment. The sample is mounted in an indium sealed Al box inside Cu a puck, which is transferred into the cryostat via a bottom loading system. Hereby both control lines (blue for gate lines and green for microwave drive lines) and readout lines (red) connect to the device.

Single qubit readout is achieved by a cavity signal reaching the transmission line. The transmitted signal is then amplified, first at base temperature via a travelling-wave parametric amplifier (TWPA), then at 4 K with a high-electron-mobility transistor (HEMT) amplifier and again at room temperature before the signal is mixed with the local oscillator. The local oscillator is detuned $\sim$ 10-50 MHz away from the cavity drive frequency and by filtering away the high frequency signal we are left with a frequency component corresponding to the detuning between the local oscillator and the drive signal. For qubit readout, two reference signals are created in software, one signal corresponding to mixing the local oscillator with the cavity drive signal and the other reference signal being $\pi/2$ out of phase. The transmission amplitude, V_H, that corresponds to the amplitude at the cavity drive frequency is extracted in software by demodulating the signal. This means that the reference signals and the transmitted signal are mixed in software leaving a DC signal and signal of twice the detuning. By a software filtering step, DC signals are extracted that correspond to the in-phase and quadrature (IQ) components of the transmitted signal. This measurement technique is called heterodyne readout and it allows readout at multiple cavity frequencies. In order to measure two qubits simultaneously two cavity drive signals detuned > 20 MHz are combined as seen in Fig. 3.3. With the exact same technique both transmission amplitudes can be probed by mixing the measurement signal at the two different drive frequencies.

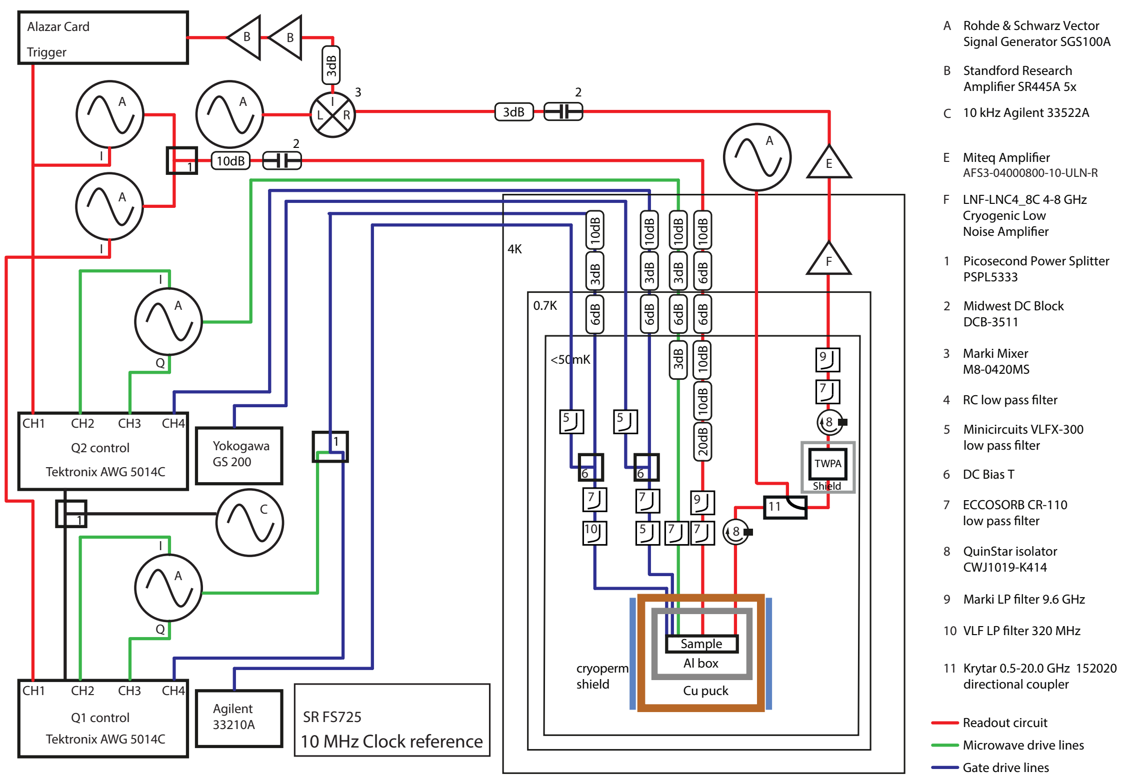

Figure 3.3: Schematics of the entire measurement setup. All electronic control equipment are connected to the SR FS725 10 MHz Clock reference. In the schematics the readout circuit is labelled in red, gate lines in blue and microwave lines in green. The only difference between the setup for Q1 and Q2 is that the microwave line is combined with the gate line of Q1 rather than going all the way to the sample through a separate line. Also note that the filtering of the gate lines of Q1 and Q2 differ with Q2 having more filtering with a lower cutoff frequency. Modified figure from [11].

3.3 TWPA

A major part of this project has been to design a new setup in a dilution refrigerator in order to implement a new near quantum limited superconducting traveling-wave parametric amplifier (TWPA) built at MIT Lincoln Laboratory [24]. Integrating the TWPA into our setup will potentially allow high fidelity readout. Achieving high fidelity single shot readout is a big challenge because of environmental noise, which is inevitable when coupling a room temperature measurement setup to a coherent quantum system. In particular thermal noise will potentially lead to decoherence as the energy scale of room temperature radiation is much larger than that of the qubit state splitting, $f_{01} \sim 5$ GHz ≈ 250 mK. Therefore careful attenuation and filtering of the drive line is needed. The sample also needs to be isolated from any noise from the amplifier stages.

The optimal power levels of the readout signal is limited by the photon occupation of the cavity [16]. If the cavity is driven at too high power the hybridisation between the resonator and the qubit disappears leaving a pure harmonic oscillator. Therefore drive power levels need to be low, which means that the transmitted signals on the qubit device are very weak and amplification of the readout signal is vital. Every component in an electronic setup is a potential noise source and to achieve high fidelity readout it is essential to introduce a minimum amount of noise during amplification. For this reason, superconducting parametric amplifiers are often integrated into the readout circuit. In general parametric amplifiers often have a narrow bandwidth [25], however the TWPA allows near quantum limited amplification over a large ~ 5 GHz frequency range. The concept of travelling wave parametric amplification is based on four wave mixing. The signal to be amplified, ω_s, is mixed with a pump signal, ω_p. The pump signal is split up and in two frequencies, an idler frequency, ω_I and ω_s. To achieve four wave mixing a circuit with a non-linearity is required, which is provided by the non-linear inductance of the JJ in the transmission line of the TWPA. The parametric gain is achieved by fulfilling both energy conservation $2\omega_p = \omega_s + \omega_I$ and phase matching of the signals. The phase matching is achieved by coupling the transmission line to lumped element resonators, which correct for any phase mismatch. Detailed descriptions of the TWPA are found in Refs. [24, 25].

The current gatemon readout scheme relies on coupling to individual resonators with unique resonance frequencies, in the two qubit device this is of course two resonators. However building a multi qubit device requires multiple unique resonators in a wide frequency range. The bandwidth and near quantum limited amplification provided by the TWPA could potentially allow high fidelity control and manipulation of many qubit systems in future experiments. The performance of the readout via the TWPA is experimentally investigated in Section 4.3.

3.4 Single line control

One of the aims of this thesis is to investigate the prospect of controlling all qubit axes through a single on chip line. In order to carry out this experiment two identical qubits (see Fig. 3.1(a)) are wired differently. Q2 is loaded into the original scheme as used in [11], where the xy-axes are controlled with a separate microwave drive line (the green line reaching the sample in Fig. 3.3). The z-axis is controlled via DC pulses on the gate line, which is heavily filtered with both an eccosorb and a 300 MHz VLFX low pass filter to minimise thermal noise reaching the sample. For controlling the xy-axes through the gate line this filtering needs to be changed to allow microwave frequencies to pass through. However just removing the VLFX filter and allowing a wide range of high frequencies to reach the qubit will possibly lead to increased decoherence. Therefore a VLF 320 MHz low pass filter is integrated, which provides much lower attenuation at the qubit drive frequencies of $\sim$ 4-7 GHz. The motivation of this filter is that most noise from higher temperature stages should be attenuated, but at the same time the reduced attenuation will allow control microwave signals to be applied. However as the attenuation characteristics of VLF filter is not completely flat in the ∼ 4-7 GHz range an extra frequency dependence of the drive power is introduced as shown in Fig. 3.4. Frequencies above the needed drive frequencies are then attenuated by the ECCOSORB CR-110 low pass filters, which are designed for filtering noise above 26 GHz.

To drive the qubit through the gate line it is required that the microwave and DC pulse signals are combined with a static DC signal, which is used for gate tuning E_J. To combine these signals inside the dilution refrigerator new bias-tees were constructed for these measurements. The bias-tees consist of a 100 kΩ resistor and a 5 nF capacitor soldered on a printed circuit board (PCB) designed to be 50 Ω matched. The bias-tees are mounted in Cu boxes and attached on the bottom plate of the mixing chamber of the dilution refrigerator for thermal anchoring.

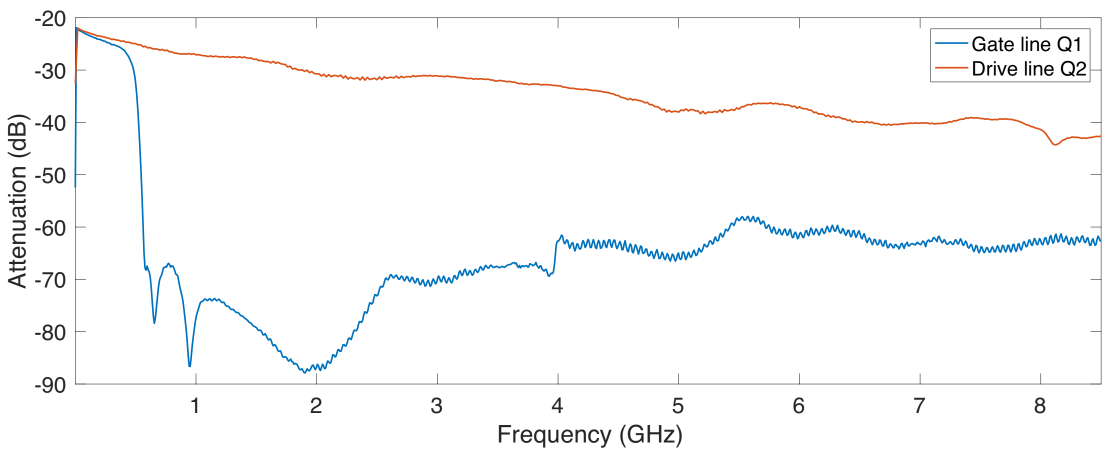

Figure 3.4: Room temperature transmission test measurements of the two lines used to control the two qubits plotted for frequencies below the cut off of the ECCOSORB filter. It is observed that the attenuation changes 10 dB on the gate line for Q1 in the qubit operational regime of ∼ 4-7 GHz. The drive line for Q2 fluctuates 2 dB in the same frequency range.

Chapter 4

Qubit measurements

This chapter presents the measurements carried out on the two qubit device shown in Chapter 3. First by presenting the basic characterisation of the qubit device, which includes measuring the cavity dispersive shift, qubit spectrum and coherence times. Hereafter the measurements that examine the performance of single line control, single shot readout and qubit feedback are presented. This is followed by measurements probing the anharmonicity with the purpose of investigating physics of the gatemon semiconducting junction. Finally two qubit measurements are shown.

4.1 Basic characterisation

Some standard characterisation experiments are always needed in a gatemon qubit experiment. Often qubit experiments begin with establishing if the qubit system and the resonator hybridise at lower cavity drive power. The dispersive shift, χ, of the resonance frequency, ω_r depends on cavity drive power such that at lower power $\chi = \frac{g^2}{\Delta}$ and at high power $\chi \to 0$ [16]. Therefore observing the power dependence of χ will indicate if the cavity is coupled to a qubit as measured in Fig. 4.1(a).

The qubit frequency, and hereby the hybridised cavity resonance frequency, can be controlled with gate voltage, V_g, and with gatemons it is natural to map out the gate dependence of χ. From capacitance simulations $g \sim 100$ MHz is expected and therefore tuning into a region of $\chi \sim 5$ MHz will correspond to $\Delta \sim 2$ GHz, from Eq. 2.9. Figure 4.1(b) shows the gate dependence of the resonance frequency of Q2. As $\chi \approx 5$ MHz at $V_g = 3$ V, this was chosen to be a good starting point for qubit measurements. Having tuned χ into a desired range, standard single qubit characterisation measurements including spectroscopy and lifetime measurements can be performed.

4.1.1 Spectroscopy

In order to locate the qubit transition frequency, f_{01}, microwave tones are applied to the qubit with varying frequency followed by a readout tone at the cavity resonance frequency. When the drive frequency matches f_{01} a shift in readout cavity transmission will be detected due to the qubit state dependent dispersive shift as explained in Section 2.2. The transition linewidth depends on the qubit drive power such that the $|0\rangle \to |1\rangle$ transition peak broadens for higher powers. For sufficiently high power multi photon transitions to higher excited states also becomes visible. Therefore

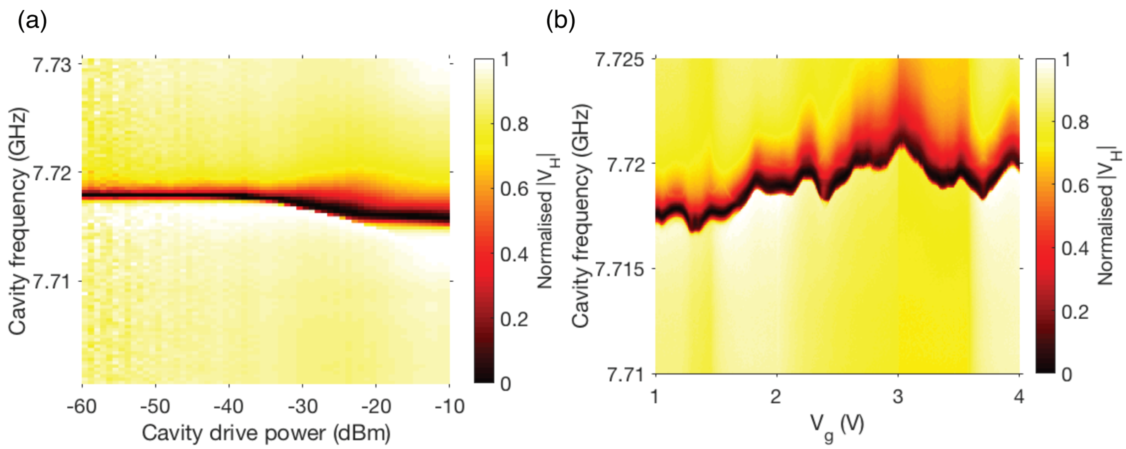

Figure 4.1: (a) Normalised transmission response, $|V_H|$ of Q2 driving the cavity resonator at different drive power performed at $V_g = 0$ V. A dispersive shift of $\chi \approx 2$ MHz is observed going from high to low power. (b) Normalised $|V_H|$ of Q2 driving the cavity resonator at -35 dBm varying V_g and drive frequency. A clear tuneability of the resonance frequency is observed.

observing the power dependence of spectroscopy peaks is often an easy way to locate f_{01}. Figure 4.2 is an example of a spectroscopy measurement, where the readout resonance frequency is calibrated firstly in (a) and in (b) the qubit drive frequency is swept, with a clear peak observed at $f_{01} = 5.12$ GHz. This characteristic qubit behaviour of broadening of the $|0\rangle \rightarrow |1\rangle$ transition peak along with a two photon $|0\rangle \rightarrow |2\rangle$ transition peak occurring as going from lower power to higher power is clearly observed in Fig. 4.2(b). The two photon transition is used in anharmonicity measurements presented in Section 4.5.

The spectrum of gatemons has been observed to be a non-monotonic function of gate voltage assigned to mesoscopic fluctuations in the nanowire [9, 11]. Therefore it is important to map out the spectrum to locate interesting regions for operations, which is achieved by spectroscopy measurements for varying gate voltages, V_1 and V_2, for both qubits. For each measurement f_{01} is extracted as in Fig. 4.2(b). It is important to drive the qubits at low enough power such that only the $|0\rangle \rightarrow |1\rangle$ transition peak is observed. Q1 was controlled through the gate line, which couples stronger to the qubit. This means that even with more wiring attenuation for Q1, a lower room temperature power is required for drive. Q1 was mostly driven at ~ -75 dBm and Q2 was mostly driven at ~ -65 dBm. However it is important to calibrate the drive power as the transition amplitudes are frequency dependent [15]. In particular for Q1 the drive power has an additional frequency dependency due to the filtering as discussed in Section 3.4. Therefore spectroscopy measurements at lower qubit frequencies were difficult as the automated spectroscopy procedure could no longer resolve the qubit frequency due to this power dependence.

The spectra of both qubits are presented in Figs. 4.3(a) and (b). Clearly there is a difference in the characteristics of the two spectra, which is consistent with every nanowire qubit being unique. The general characteristics of the qubit spectra were observed to be constant in these experiments even

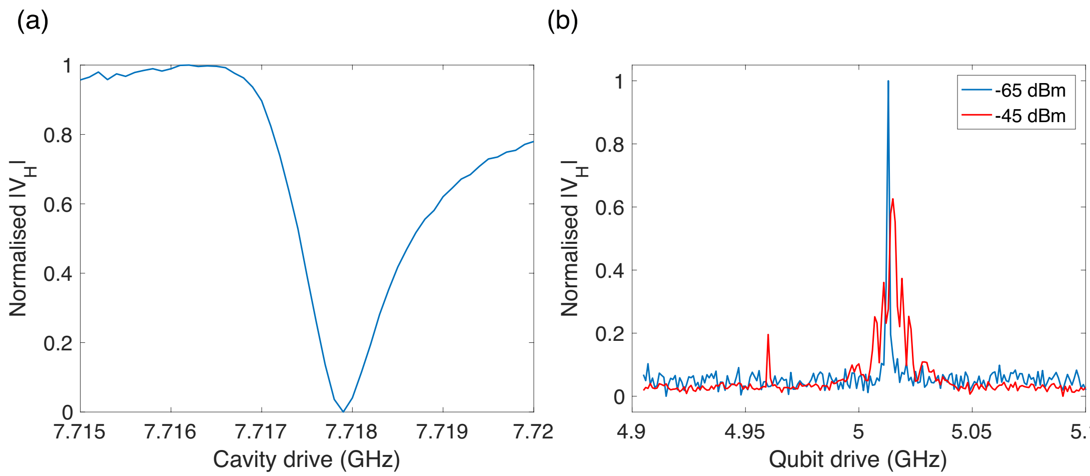

Figure 4.2: (a) Measurement of the cavity resonance frequency at a gate voltage of 0.65 V. (b) Examples of two spectroscopy measurements where the qubit is driven by a 3 μs wide microwave pulse at -65 dBm (blue) and -45 dBm (red). In this case $f_{01} = 5.01$ GHz. Driving at the higher power a second transition peak is observed at 4.96 GHz as well as a broadening of the $|0\rangle \rightarrow |1\rangle$ peak. The transmission signal, V_H is normalised with respect to the measurement at -65 dBm.

though they might drift in gate voltage, which is consistent with previous gatemon experiments [11]. The unique and non-monotonic behaviour of the qubit spectra are not desired properties of a qubit system but mapping out each qubit spectrum allows suitable regions for qubit operation to be identified.

4.1.2 Basic control

When talking about qubit systems a key question is of course how controllable the system is. Superconducting qubits are controlled with microwave pulses that allow rotations to all points in the qubit subspace. Trying to apply qubit manipulations is an efficient way to ensure that a controllable two-level system has been located. In particular testing if Rabi oscillations can be induced is a clear way of establishing the controllability of a qubit system. These oscillations are coherent rotations around the x-axis. By applying a microwave tone at the qubit transition frequency with varying pulse length, τ, the qubit state vector will oscillate around the x-axis corresponding to the rotation labelled R_X^θ in Fig. 4.4(a). An example of a Rabi measurement is shown in Fig. 4.4(b). Rabi oscillations can also be driven around the y-axis by simply applying the microwave pulses $\pi/2$ out of phase in IQ-space due to the drive term of the Hamiltonian. Rabi measurements are also used to calibrate π and $\pi/2$ pulses, as needed, for instance, for coherence measurements.

The Ramsey measurement, where the qubit vector is set to oscillate around the z-axis on the Bloch sphere, is another important characterisation experiment. By applying a $\pi/2$ pulse at a drive

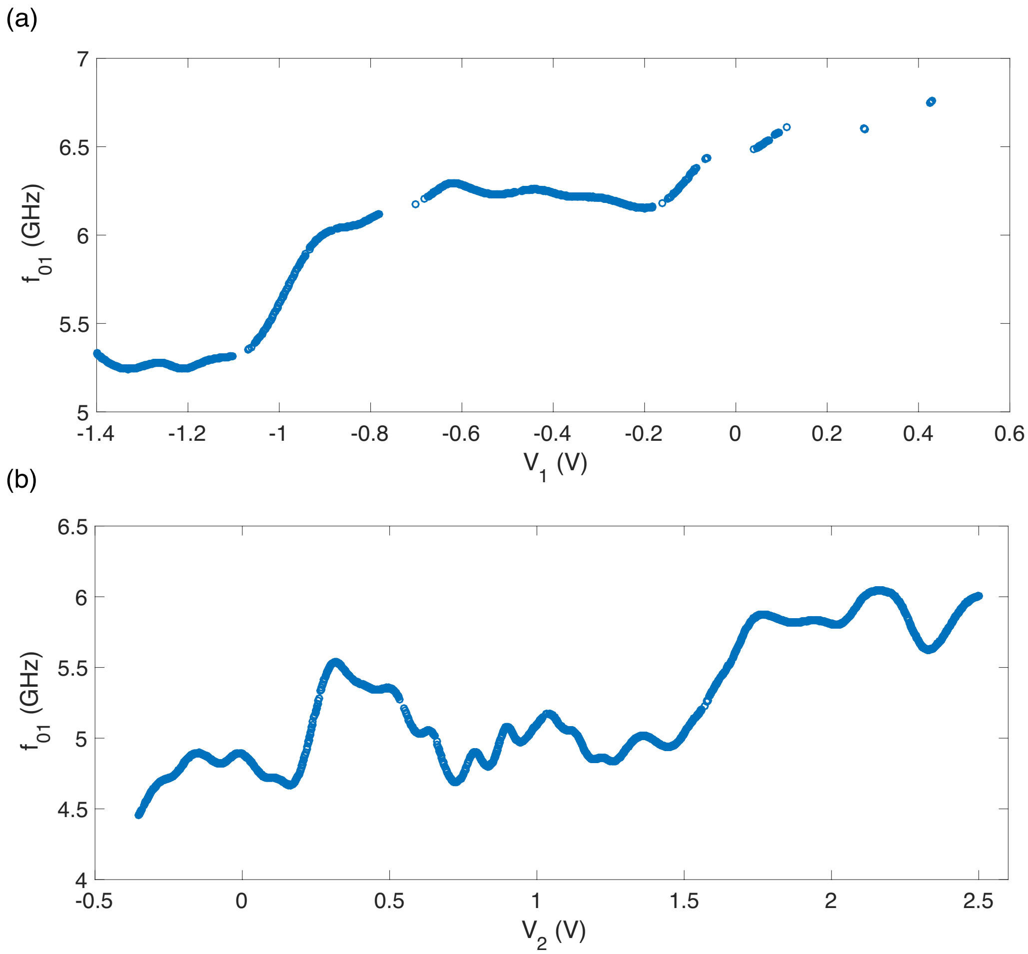

Figure 4.3: Spectrum of qubit transition frequencies, f_{01}, measured as a function of gate voltage for both qubits. a) Spectrum of Q1 as function of gate voltage, V_1. b) Spectrum of Q2 as a function of gate voltage, V_2.

frequency, f_d, that is slightly detuned (a few MHz) from the qubit resonance the qubit state will precess on the Bloch equator at this detuning frequency, $\Delta_q/2\pi = |f_{01} - f_d|$ due to the drive term in the Hamiltonian as seen in Section 2.2. After a certain delay time, τ, the state vector is projected onto the z-axis with another $\pi/2$ pulse. The population of $|0\rangle$ and $|1\rangle$ will then depend on the precession angle, and will oscillate between maximum $|0\rangle$ population and maximum $|1\rangle$ population as shown in Fig. 4.4(c). In the Rabi measurement the transmission data is converted to an excited state probability, $P_{|1\rangle}$, by fitting the data with $A\sin(\omega t + \phi)\exp(-t/T) + b$. The procedure assumes that there is no leakage to higher states. On the other hand in the Ramsey measurement the normalised transmission amplitude, V_H, is not converted to a probability. In these units, the value 1 corresponds to maximum $P_{|1\rangle}$ and 0 corresponds to minimum $P_{|1\rangle}$. The Rabi measurements demonstrate coherent XY control of the qubit and the Ramsey measurement is an important tool used, for instance, to characterise coherence and track the qubit frequency.

Controlling the z-axis in gatemons exploits the same mechanism that causes qubit precession in a Ramsey measurement. Applying a $\pi/2$ pulse exactly on resonance with the qubit will bring the state vector to the equator of the Bloch sphere. Then applying a DC square pulse with amplitude ΔV_g and width τ will detune f_{01} and therefore cause state precession. Projecting the state vector onto the z-axis with another $\pi/2$ pulse in the same way as in the Ramsey experiment will produce oscillations in the state populations depending on the width and amplitude of the gate pulse, see Fig. 4.4(d). It is worth noting that this way of controlling the z-axis with a gate pulse is unique to gatemons as conventional transmon tune f_{01} with magnetic fluxes. However the origin of the z-oscillations are exactly the same as described by the $\hat{\sigma_z}$-term in the Hamiltonian (Eq. 2.10).

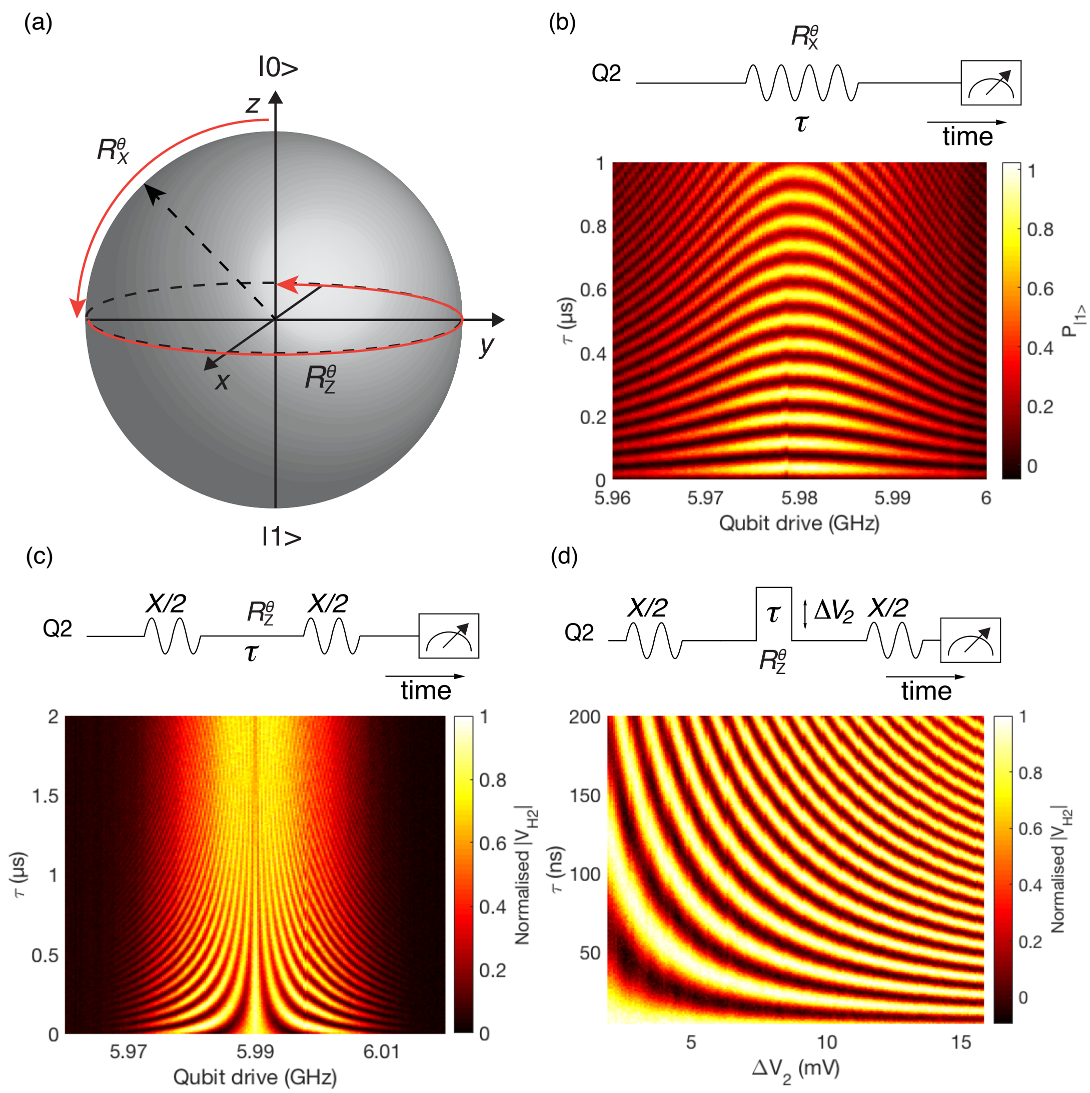

Figure 4.4: (a) Bloch sphere description of the single qubit subspace. The arrows indicate x- and z-rotations for a certain angle, θ, illustrating either the Rabi or Ramsey oscillations. (b) Pulse sequence and data for a Rabi measurement on Q2. The qubit is driven by a microwave pulse of varying frequency and width, τ, causing oscillations around the x-axis. The cavity transmission is read out after the pulse. The colour scale shows the state probability of $|1\rangle$ defined by fitting a damped sinusoid to the data. (c) Pulse sequence and data for a Ramsey measurement on Q2. The qubit is prepared on the Bloch equator with an X/2 pulse (a $\pi/2$ pulse around the x-axis) calibrated from the Rabi experiment. After a delay time, τ, the qubit is projected onto the z-axis with another X/2 pulse. The cavity transmission is read out after the X/2 pulse. The colour scale shows the normalised transmission voltage, V_{H2}. (d) Pulse scheme and data for coherent Z oscillations. The qubit is prepared on the equator of the Bloch sphere with an X/2 pulse. With a DC square pulse of varying amplitude, ΔV_2, and width, τ the qubit is detuned from the drive frequency and the state vector will precess a certain angle around the z-axis depending on ΔV_2 and τ. Projecting the qubit state onto the z-axis with another X/2 pulse as in the Ramsey experiments will lead to oscillations in the qubit state population.

4.1.3 Coherence times measurements

When describing qubit systems, coherence times are obvious key parameters, which need to be quantified. Coherence is commonly quantified by two characteristic time scales, T_1 and T_2^*. T_1 is the characteristic time scale of the exponential qubit decay from $|1\rangle$ to $|0\rangle$. A T_1 measurement is performed by driving the qubit from $|0\rangle$ to $|1\rangle$ with a π pulse calibrated from a Rabi measurement. By stepping the delay time, τ, between the π pulse and the readout pulse the probability of the qubit having decayed will increase. An example of a T_1 measurement is shown in Fig. 4.5 (a), where each data point corresponds to 1000 measurement points averaged together. This means that the qubit is prepared in $|1\rangle$ with a π pulse and read out a 1000 times per data point. V_H is linearly dependent on the qubit state probability and by fitting an exponentially decaying function to the data T_1 is extracted. In order to extract T_2^* a Ramsey measurement is carried out. The state population will oscillate with an amplitude that decays on a characteristic time scale T_2^*. Here, T_2^* is obtained by fitting $A\sin(2\pi\Delta_q t + \phi)\exp(-t/T_2^*) + b$ to the cavity transmission data.

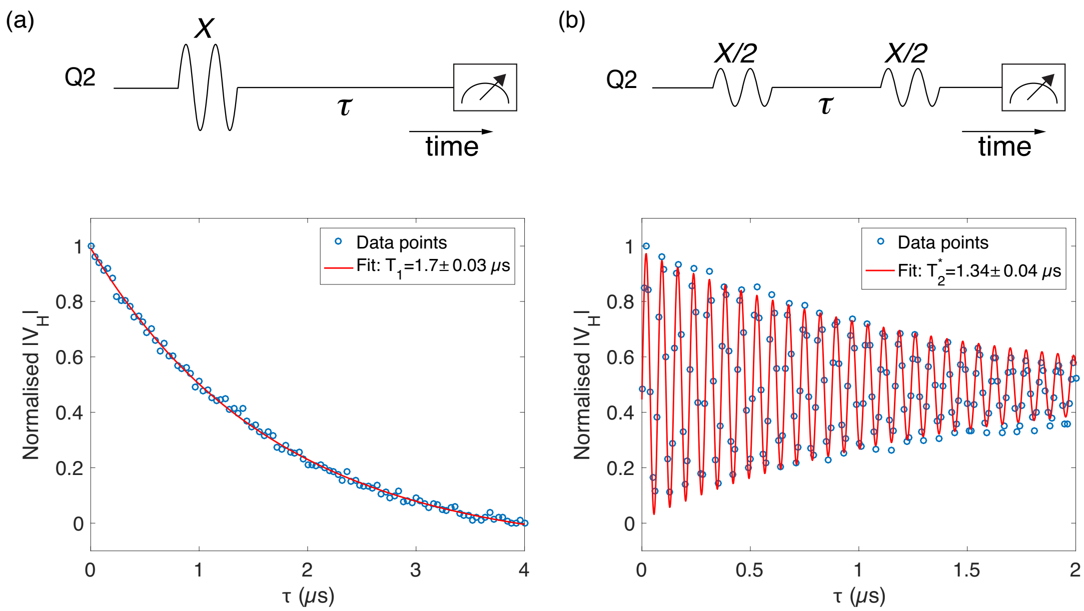

Figure 4.5: Coherence time measurements performed at $V_g = 3$ V and a qubit drive frequency of 6 GHz. (a) Pulse scheme and data for a T_1 measurement on Q2. The qubit is prepared in $|1\rangle$ with an X pulse and the cavity transmission signal, V_H is readout after varying the delay time, τ. Each data point corresponds to 1000 averaged measurement points. By fitting $A\exp(-t/T_1) + b$ to the data T_1 is extracted. In this case $T_1 = 1.70 \pm 0.03$ µs is measured. b) The pulse scheme together with the measurement data for a T_2^* measurement on Q2. The sequence is exactly a Ramsey pulse sequence. As with the T_1 measurement each data point corresponds to 1000 pulse sequences. By fitting $A\sin(\omega t + \phi)\exp\left(-t/T_2^*\right) + b$ to the data T_2^* is extracted. In this case $T_2^* = 1.34 \pm 0.04$ µs is measured.

4.2 Single line control

A great challenge scaling any qubit system is scaling the control electronics. Obviously the simpler it is to control a single qubit the less challenging it will be to scale control electronics for many qubit systems. Therefore an aim of this project has been to investigate the possibility of controlling all three qubit axes through a single on-chip control line instead of having separate control lines for XY and Z control as in previous gatemon experiments [11].

Of course reducing the number of control lines is only desirable if coherence times of the qubit system will not be degraded. In order to quantify the influence of the control lines, the two-qubit sample (Fig. 3.1(a)) was loaded with each qubit having different wiring and filter configurations, see Section 3.2 for details. The two qubits are designed and fabricated to be identical to the extent that the random positions of the nanowires allow and therefore this experiment should give an indication whether single line control will be applicable for future gatemon qubit designs.

Before quantifying the performance of the qubit it is first necessary to establish that qubit control with a single line is just as easy as qubit control with separate XY and Z lines. In Fig. 4.6(a) Rabi measurements driven through the gate line are shown for Q1. The measurement is performed as on Q2 except driving through the gate line and not through the separate microwave drive line. In Fig. 4.6(b) coherent Z oscillations, also driven through the gate line, are shown for Q1. This shows that all qubit axes can be controlled via the gate line with equal ease as in the original configuration. Having established that basic operations through the gate line are possible, coherence times of the

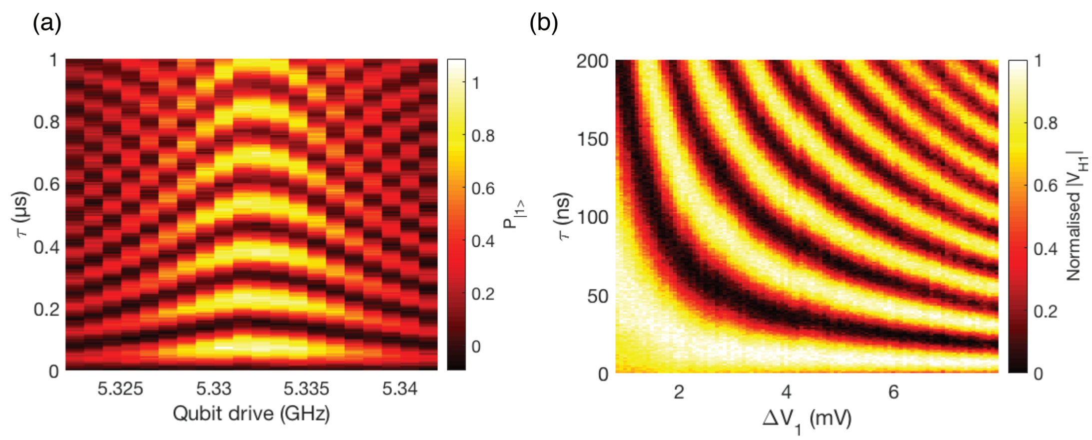

Figure 4.6: (a) Rabi oscillations measured on Q1 performed using exactly the same pulse scheme as for Q2 except that the qubit is driven through the gate line with a −50 dBm pulse. The colour scale shows $P_{|1\rangle}$. (b) Coherent Z oscillations on Q1 driven by applying DC pulses through the single line. Pulse schemes are shown in Fig. 4.4.

two qubits are investigated over broad frequency ranges. These measurements are performed by an automated procedure that calibrates the readout frequency at each gate voltage. f_{01} is then located with a spectroscopy scan followed by T_1 and T_2^* measurements. Using the exact same fitting procedure as in Figs. 4.5(a) and 4.5(b) the coherence times are extracted for each gate voltage and hereby for different qubit frequencies. In Figs. 4.7(a) and 4.7(b) measurements of coherence times are shown for both qubits over a ~ 2 GHz range. As the qubit spectra are unique (see Figs. 4.3(a) and 4.3(b)) it is difficult to map the coherence times in exactly the frequency same range, which would have been preferred for comparison. The coherence times measured on the two qubits are

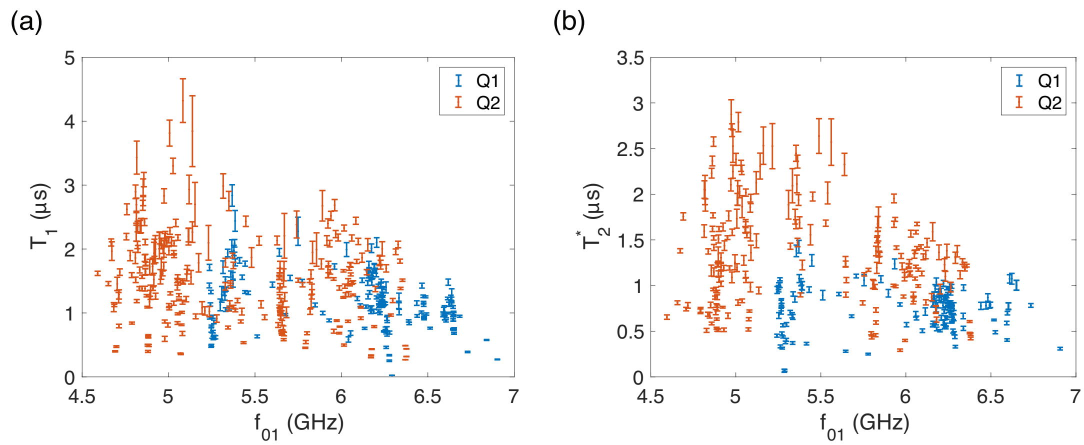

Figure 4.7: Coherence time measurements plotted against qubit transition frequency, f_{01}. (a) T_1 measurement results. (b) T_2^* measurement results.

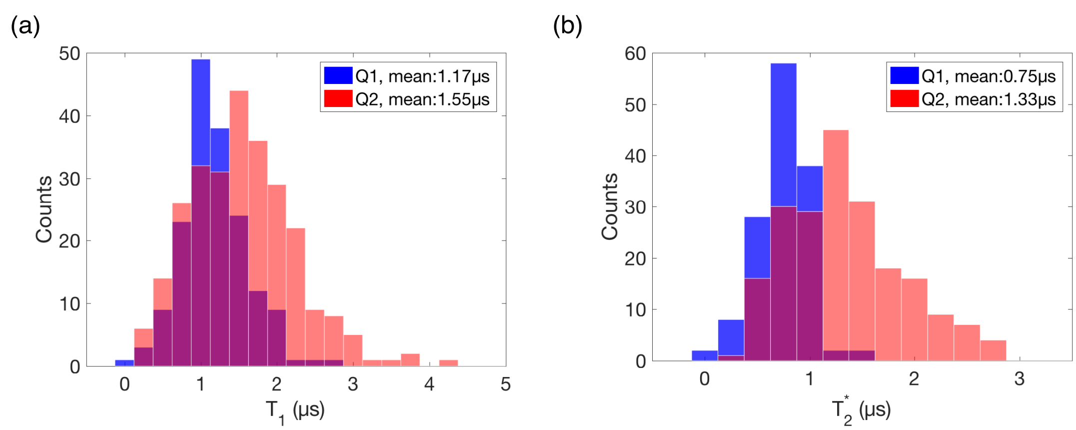

Figure 4.8: Histogram of coherence time measurements obtained for Q1 and Q2 measured over a frequency range of 2 GHz. (a) T_1 measurement results. (b) T_2^* measurement results.

of the same order of magnitude with Q1 consistently showing slightly lower coherence times compared to Q2. However it is difficult to quantify whether this is due to variations in the two qubits or because of additional high frequency noise allowed to reach Q1 compared to Q2. For better comparison it would have been interesting to reload this device with the wiring of the two qubits exchanged. Repeating the coherence measurements would then allow comparing the two qubits to themselves.

An observed difficulty of the single line control is that the drive power level is much more frequency dependent due to the larger ripples in transmission characteristics of the line filtering. In future experiments this can most likely be avoided by calibrating the drive power from transmission data as shown in Fig. 3.4 or preferably by low temperature transmission calibration measurements.

To really quantify the performance of the single line control more qubit measurements would be needed, such as benchmarking of gate operations. Also to really make the single line control interesting it would have to be demonstrated on qubit devices with longer life times. Nevertheless these measurements do not rule out that future qubit device designs can be based on single line control and encourage further work.

4.3 Single shot readout

An important requirement for gatemons to become a candidate for quantum computation is accurate measurement of qubit states with a single shot. Fault tolerant code schemes need both entangling quantum operations and precise state measurements [26]. Also implementing full tomography schemes for gatemons requires single shot state identification as entangled qubit correlations cannot be determined from average measurements [16].

With the new electronics setup including a near quantum limited amplifier, see Fig. 3.3, high fidelity single shot readout is potentially allowed. In order to test and optimise the readout, experiments preparing the qubit in either $|0\rangle$ or $|1\rangle$ are conducted. In this case preparing the qubit in the ground state does not take excited state equilibrium population into account. Preparing the qubit in $|1\rangle$ is achieved by applying a π pulse calibrated in a Rabi experiment. The raw IQ-data of 10^4 such measurements points for each prepared qubit state is shown in Fig. 4.9(a). These IQ-data are used to create histograms of the two prepared states. This is done by projection the data on to the line that provides largest separation between the two IQ-clouds. The probability of measuring the $|0\rangle$ and $|1\rangle$ qubit preparations correctly is known as the readout fidelity, which is quantified by discretely integrating the histograms in Fig. 4.9(b) by taking the cumulative sum and normalising the sum to the number of measurement points as shown in Fig. 4.9(c). The readout fidelity is then identified as the maximum separation between the two curves in Fig. 4.9(c), where a separation of 70% is found. The value of I' providing the largest separation will then act as a threshold to determine the qubit state in a single measurement. These measurements were repeated for varying values of the integration time, integration delay time, cavity drive frequency and power to find the optimal parameter values that allow the highest possible fidelity.

Before collecting the single shot data, a T_1-measurement is performed, showing $T_1 = 1.6 \pm 0.03$ µs. The large population of prepared $|1\rangle$ measurements overlapping with prepared $|0\rangle$ measurements in Fig. 4.9(b) is clearly caused by decay during the 1 µs integration time. This is completely expected from a simple estimate of the expected error due to relaxation based on the measured T_1 and the integration time, t_m,

$$\int_0^{t_m/2} \frac{1}{T_1} e^{-t/T_1} dt = 1 - e^{-t_m/2T_1} = 0.27. \tag{4.1}$$

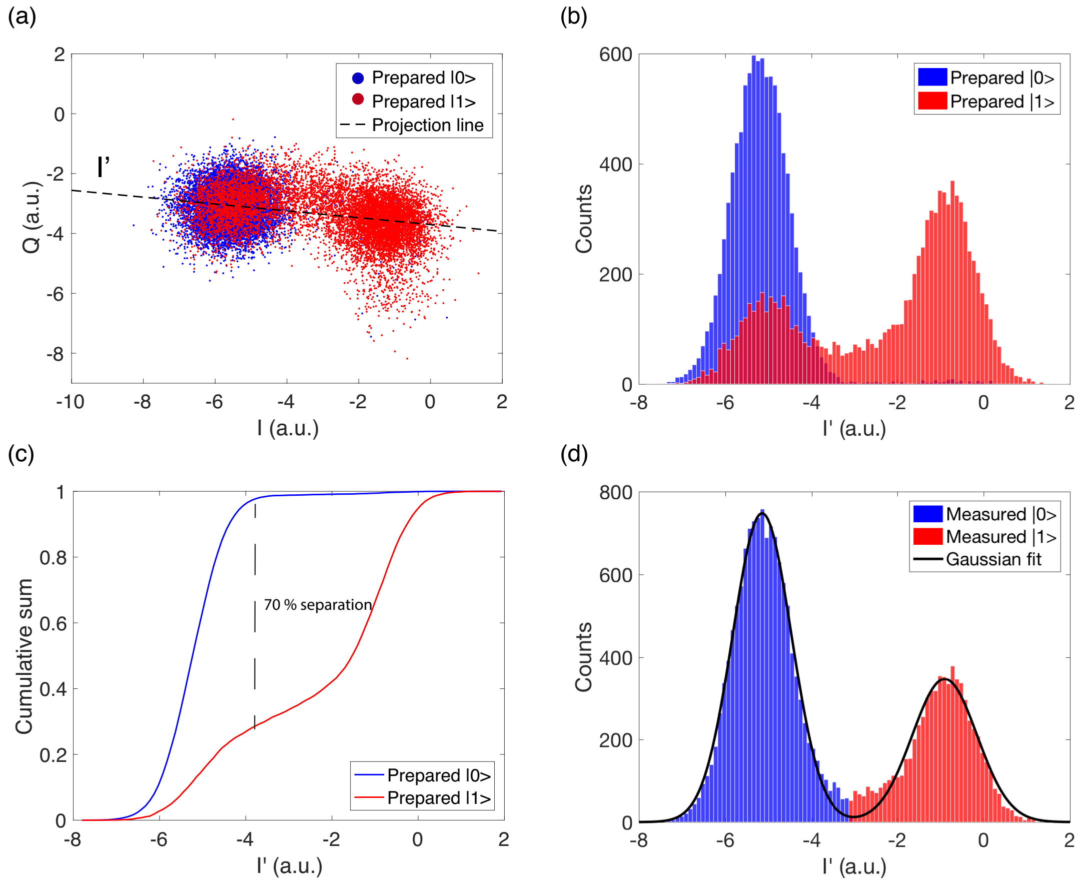

Figure 4.9: Single shot readout performance measurements. (a) Raw IQ-transmission data. The blue cloud shows the single shot measurements of the qubit prepared in $|0\rangle$ and the red cloud shows the single shot measurements of the qubit prepared in $|1\rangle$. The black dashed line shows the line of projection, which will provide largest separation of the two IQ-clouds. (b) Histograms of the distributions of the single shot measurements projected onto the dashed line in (a). The blue histogram shows the single shot measurements of the qubit prepared in $|0\rangle$ and the red histogram shows the single shot measurements of the qubit prepared in $|1\rangle$. It is observed that the histogram for the qubit prepared in $|1\rangle$ has two peaks indicating large error due to decay. (c) The cumulative sum of both histograms in (b) normalised to the number of measurement shots. The readout fidelity is quantified as the maximum probability of identifying the prepared $|0\rangle$ and $|1\rangle$ data correctly, labelled as the dashed line. In this measurement the readout fidelity is 70 %. (d) Histogram of combined $|0\rangle$ and $|1\rangle$ data. $|0\rangle$ and $|1\rangle$ measurements are distinguished from each other by fitting two Gaussians to the entire data set and setting a threshold that provides the lowest total error probability.

The integral only goes to $t_m/2$ because of the assumption that a signal from a state that is $|1\rangle$ for more than half of the measurement time will lead to a $|1\rangle$ detection.

Instead of separating the data by which state the qubit was prepared in the data can be separated into which state was actually measured. This is done by fitting a sum of two Gaussians to the entire IQ-data regardless of the prepared state and then setting a threshold, which decides whether a measurement is detected as a $|0\rangle$ or $|1\rangle$ as shown in Fig. 4.9(d). The threshold, x_0, is set as the point, where the two Gaussians intersect as this point minimises the total error probability. The separation fidelity, F_s, is defined as the mean probability that a measurement from either distribution is identified correctly and is given by integrating either Gaussian to the threshold [27],

$$F_s = \frac{1}{2}\left(\int_{-\infty}^{x_0} \frac{1}{\sqrt{2\sigma_0^2\pi}} e^{-\frac{(x-\mu_0)^2}{2\sigma_0^2}} dx + \int_{x_0}^{\infty} \frac{1}{\sqrt{2\sigma_1^2\pi}} e^{-\frac{(x-\mu_1)^2}{2\sigma_1^2}} dx\right) = 98.2\%. \tag{4.2}$$

From the single shot measurements it is clear that the short lifetimes of the qubits are the main obstacle achieving high readout fidelity with $> 90\%$ of the readout errors being caused by relaxation. It is obvious that by either raising T_1 or lowering the measurement time without decreasing the separation fidelity would improve readout. Particularly improving gatemon coherence is an important aim for future experiments. In addition to improving qubit lifetimes it would also be advantageous to reduce the integration time and delay time before integrating. In particular it would be interesting to examine different readout pulse shapes rather than square pulses with Gaussian rise and fall used so far to achieve the higher separation fidelity. Inspired by [26] the readout can be improved by investigating pulse shapes where the resonator is rung up with an initially strong pulse, which decays with $1/\kappa_r = \frac{\omega_r}{Q}$. Here Q is the external coupling quality factor of the resonator to the transmission line. Previous experience in our subgroup suggests that resonators fabricated the same way as in this experiment have $Q \sim 10^4$. With such a high Q-factor the resonators require long ring up time and it seems obvious that the square pulses are not the most efficient. In present measurements a delay of ~ 300 ns is typically applied to accommodate the ring up time, which means that the qubit has significant time to decay before the measurement signal is even recorded. Even though further improvement of the fidelity is possible, short coherence times are presently the main bottleneck and will be the main priority towards improving readout.

4.4 Feedback

Throughout measurements of this device fluctuations in the qubit frequency are observed. Previous gatemon experiments have shown that the qubit frequency is very stable over long time scales when operating at sweet spots in the qubit spectrum [11]. Although this provides sufficient stability to do coherent gatemon control it is preferable to be able to operate the qubit anywhere in the spectrum. In particular entangling gates such as the $\sqrt{\text{iSWAP}}$ (see Section 4.6) require operations to be at steep regions in the spectrum that allow gate pulses to tune the qubit frequency in a range of 100-500 MHz range. Additionally it is unlikely that when scaling these systems the unique spectrum of each qubit will be compatible with sweet spot operation. For that reason efficient feedback to stabilise the qubit frequency is desired and therefore simple feedback schemes have been implemented on this device.

The Ramsey measurement is a very precise way of tracking the qubit frequency, in fact Ramsey measurements are used in atomic clocks to probe transition frequencies. As explained in Section 4.1.2, $\Delta_q = |\omega_d - \omega_{01}|$, is the frequency of the Ramsey oscillations and by fitting a sinusoid to the oscillations, Δ_q can be extracted from the Ramsey experiment and therefore also f_{01}. In this experiment it is sought to lock Δ_q at 5 MHz, which is done by correcting the gate appropriately. As we have seen that the gate spectrum is very irregular, a local gate spectrum around the qubit operation is obtained to provided a proportionality constant between gate voltage and qubit frequency. Figure 4.10(a) presents Ramsey data used to track the qubit frequency when not applying feedback. The data are obtained by repeating Ramsey measurements in real time, t. Δ_q is extracted by fitting $A\sin(\Delta_q t) + b$. Figure 4.10(b) presents the Ramsey data used to extract Δ_q in the case of applying feedback. Already from these two figures it is clearly observed that the feedback is able to lock into a particular frequency with the exception of when there are sudden jumps in the frequency. Figure 4.10(c) shows an example of how the frequency is extracted for every single Ramsey measurement in order to estimate Δ_g as function of time, which is then shown in Fig. 4.10(d). It is clearly demonstrated that the feedback mechanism is able to lock into a specific qubit frequency. However this simple feedback scheme is rather slow as each Ramsey trace uses 200 points averaged 500 times each to obtain a Δ_q value. Each Δ_q measurement takes around 8 s. For future applications one can imagine running an algorithm that performs a series of computational gates and within every cycle the feedback procedure is run. For that matter a faster method is preferred but this first implementation serves as a demonstration that gate feedback is definitely possible for gatemon qubits encouraging further work on more sophisticated feedback schemes.

4.5 Anharmonicity

The development of the gatemon qubit is in many ways built on existing fabrication, measurement and control techniques for conventional transmons. As mentioned the fundamental difference between the two qubit types is the way of constructing the Josephson junction. Building a qubit based on a semiconductor junction rather than an insulator junction however might introduce physical differences between the two systems.

Indications of reduced anharmonicity, α, were discovered in the previous gatemon measurements [9], where the measured α was significantly lower than the theoretically predicted $\alpha/h \approx -E_c/h \approx -200$ MHz as estimated from electrostatic simulations. A lowered anharmonicity can be explained from a model, where the nanowire junction consists of few highly transmissive channels instead of many low transmissive channels in the case of the insulating junction. A simple model was developed in collaboration with local theorists Michael Hell and Martin Leijnse, which explains the lowered anharmonicity by the enhanced transmission probabilities. Anharmonicity measurements were performed at varying gate voltages on both qubits to test the transmission model. To probe the anharmonicity high power spectroscopy measurements were conducted. This way two-photon virtual transitions to higher states are possible as the probability amplitude of the $|0\rangle \rightarrow |2\rangle$ transition is enhanced to be measurable. At the same time the $|0\rangle \rightarrow |1\rangle$ transition peak will broaden. With this characteristic behaviour spectroscopy measurements at high power provides an efficient way to identify the two transitions and thereby quantify α. As described in Section 2.1 α is negative for transmons as a consequence of the enlarged $\frac{E_J}{E_C}$ ratio. Therefore the $|0\rangle \rightarrow |2\rangle$ peak will occur at a lower frequency than the $|0\rangle \rightarrow |1\rangle$ peak, which can be seen from,

$$0 > \alpha = E_{12} - E_{01} = E_{02} - 2E_{01} = 2h\left(\frac{f_{02}}{2} - f_{01}\right) \Rightarrow f_{01} > \frac{f_{02}}{2}, \tag{4.3}$$

where E_{ij} and f_{ij} are the transition energies and frequencies. An example of a spectroscopy measurement to extract α for a given V_g, is shown in Fig. 4.11(a). The data are obtained by recording

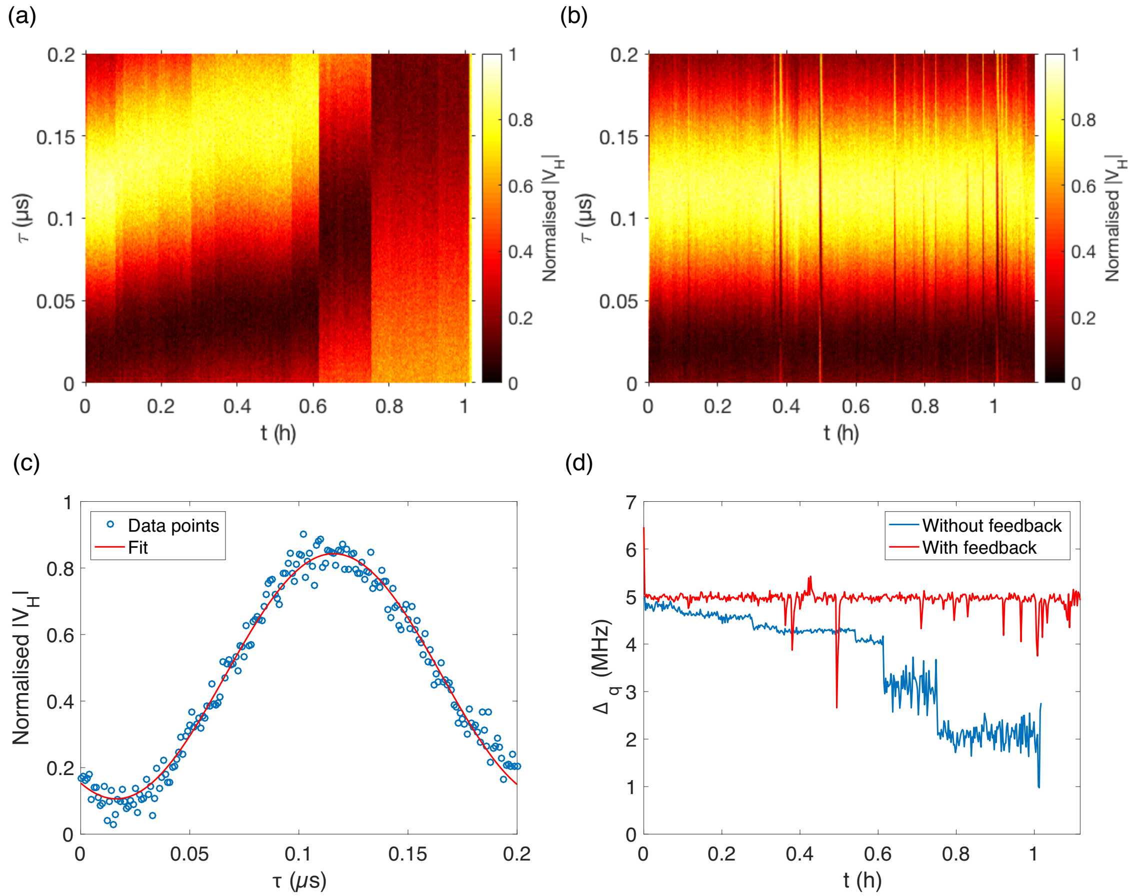

Figure 4.10: Qubit frequency tracking and stabilisation. (a) Raw Ramsey data for the measurement, where feedback is not applied. Each Ramsey measurement is performed at the same drive frequency with τ varying from 0-200 ns in 200 steps. To track the qubit frequency the measurements are repeated in different points in time, t. (b) Same as (a) except feedback is now on after each Ramsey measurement, where Δ_q is extracted and the gate voltage is stepped such that $\Delta_q = 5$ MHz is locked. The proportionality constant between gate voltage and qubit frequency is in this measurement 0.3 $\frac{\mathrm{V}}{\mathrm{GHz}}$. (c) Linecut of (a) at $t = 200$ s to illustrate how Δ_q is extracted. The Ramsey measurement is fitted with $A\sin(\Delta_q t) + b$ and in this case $\Delta_q = 4.75 \pm 0.04$ MHz is found. (d) Δ_q as a function of t with (red) and without (blue) feedback, where each point is extracted as in (c). It is observed that the feedback manages to lock into a detuning of 5 MHz except when there are sudden jumps.

$|V_H|$ while sweeping V_g and the qubit drive frequency. By fitting the spectroscopy data at each value of V_g with a sum of two Gaussians, the means of the Gaussian are identified as the transition frequencies, f_{01} and $\frac{f_{02}}{2}$. The reason for the factor 1/2 is that the transition is a two photon process. In the example shown in Fig. 4.11(b) the frequencies extracted from the fit are, $f_{01} = 5.3041 \pm 0.0002$ GHz and $\frac{f_{02}}{2} = 4.9691 \pm 0.0003$ GHz, leading to an extracted $\alpha = 2\left(f_{01} - \frac{f_{02}}{2}\right) = 130.0 \pm 0.7$ MHz. Repeating these measurements for a broad gate voltage range on both qubits allows the anhar-

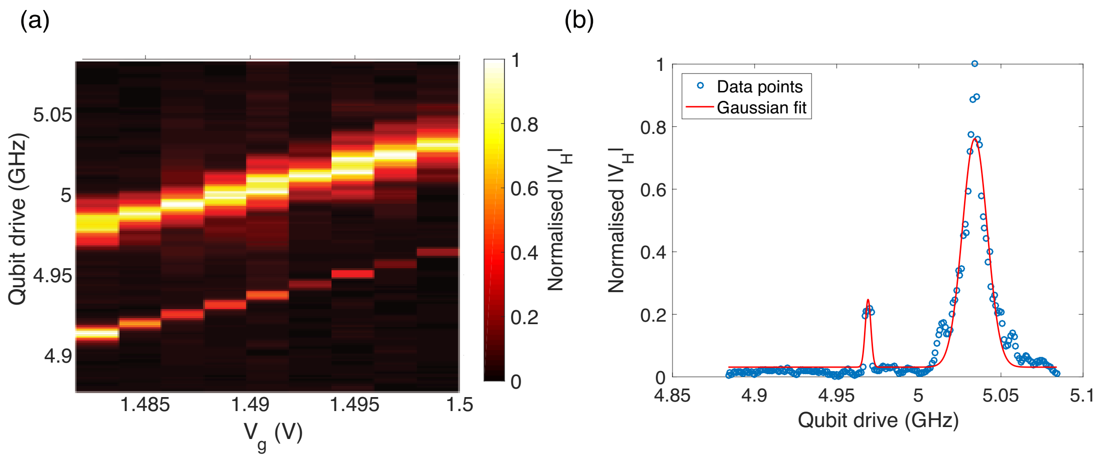

Figure 4.11: Example of an anharmonicity measurement on Q2. (a) Spectroscopy measurement driving Q2 at -45 dBm. The gate is stepped 20 mV in 10 steps and for each gate value the qubit is driven with a drive frequency in a 200 MHz range. (b) Normalised $|V_H|$ plotted against drive frequency at $V_G = 1.5$ V. The data are fitted with a sum of two Gaussians to resolve the two peaks and the means of the Gaussians are identified as f_{01} and $f_{02}/2$. In the case $f_{01} = 5.3041 \pm 0.0002$ GHz and $\frac{f_{02}}{2} = 4.9691 \pm 0.0003$ GHz.

monicity spectrum to be mapped out. The results of these measurements are shown in Fig. 4.12(a) for Q1 and (b) for Q2. Each data point is extracted with the same fitting method used in Fig. 4.11(b). These measurements were performed with an automated process that locates f_{01} at lower drive power (-65 dBm in the shown example) in the same way as in Fig. 4.2(b). After this the T_1, T_2^* and α measurements were carried out. However as the drive power needed to probe the $|0\rangle \rightarrow |2\rangle$ transition is frequency dependent the automated measurement procedure lost track of the qubit transitions for some of the gate values. In particular this was a challenge when measuring Q1 due to ripples in the control line transmission, as discussed previously. Therefore the gate range of spectroscopy and anharmonicity measurements are shorter on Q1 compared to Q2.

From the results it is clear that anharmonicity is certainly not constant in V_g as with conventional transmons but rather a continuous, non-monotonic function of V_g. From simulations $E_C \approx$ 200 MHz, which is believed to be reliable as other simulated quantities such as the qubit-resonator and qubit-qubit coupling are consistent with measured values. The reduced absolute value of the anharmonicity, fluctuating in the range of 50-150 MHz compared to the simulated $E_C \approx 200$ MHz is a clear indication that gatemons and transmons cannot be considered to be completely identical systems. Also the lowered anharmonicity is consistent with the enhanced transmission of the junction channels, but it is difficult to conclude anything quantitative about the functional form of α. I speculate that the fluctuations in α are governed by the same fluctuations that determine the shape of the qubit spectra, but it is important to note that frequency and anharmonicity are not correlated over the entire spectrum. The anharmonicity of a qubit system sets a bound on how fast qubit gates can be and the lower the anharmonicity the higher is the risk of leaking into non computational states. Therefore with a variation of ≈ 100 MHz from the highest to the lowest values on α it is important to tune into a region of high α before operating the qubits.

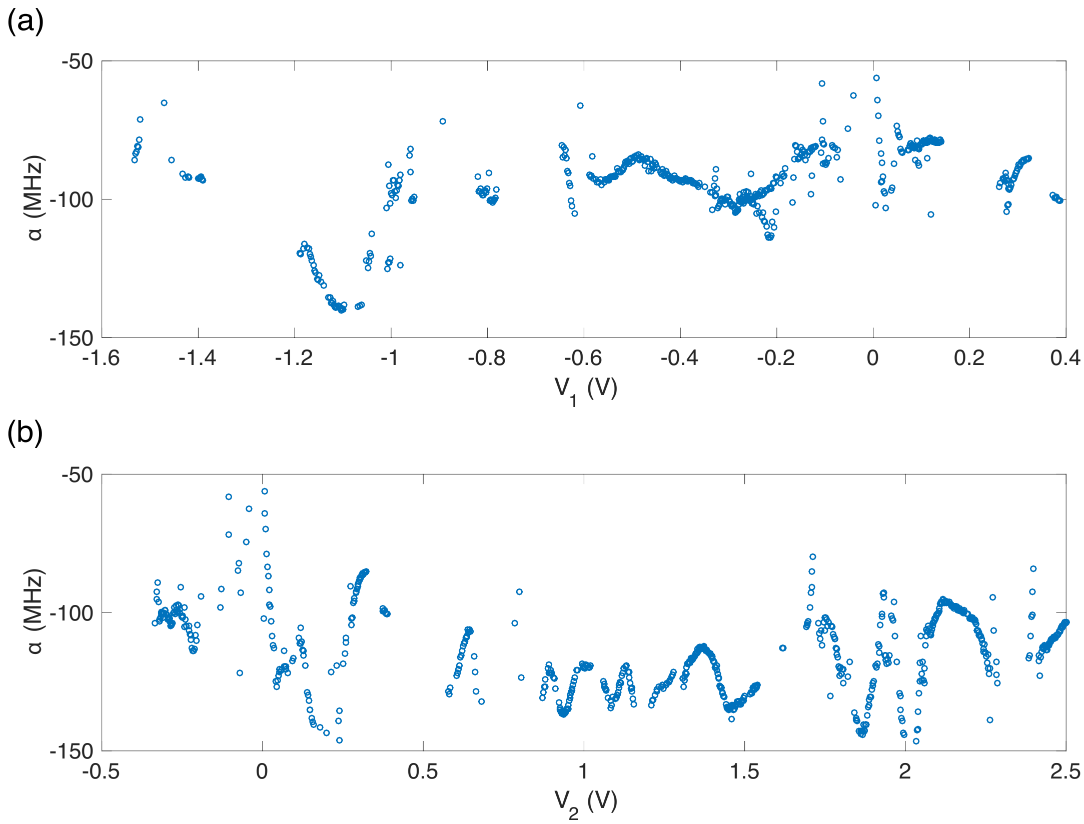

Figure 4.12: Anharmonicity measurements on both qubits. (a) Anharmonicity, α, plotted as a function of gate voltage, V_1, on Q1. (b) α plotted as a function of gate voltage, V_2, on Q2.

4.6 Two qubit measurements

Being able to coherently couple qubits is essential for a quantum processor. Nearest neighbour coupling in superconducting devices has proven to be easily engineered via capacitances. As shown in Fig. 3.1(a) the two qubit islands are closely spaced and the capacitance between the island determines the coupling. As discussed in Section 2.2.2 the qubit-qubit coupling is only present when the qubit frequencies are near each other. In a very simplified picture it can be understood as the Hamiltonian changing from two uncoupled single qubit systems to a coupled two qubit system, when the qubits are brought to resonance,

$$\begin{pmatrix} \hbar\omega_{01}^{(1)} & 0 \\ 0 & \hbar\omega_{01}^{(2)} \end{pmatrix} \rightarrow \begin{pmatrix} \hbar\omega_{01} & \hbar g_q \\ \hbar g_q & \hbar\omega_{01} \end{pmatrix}, \tag{4.4}$$

where $\omega_{01}^{(1)}$ and $\omega_{01}^{(2)}$ are the qubit transition frequencies for Q1 and Q2 respectively and ω_{01} is the common transition frequency, when tuned into resonance. The eigenfrequencies change from $\omega_{01}^{(1)}$ and $\omega_{01}^{(2)}$ to $\omega_{01} \pm g_q$, which explains the avoided crossing observed in the two qubit spectroscopy measurement shown in Fig. 4.13(a). In this measurement Q1 is parked at $\frac{\omega_{01}^{(1)}}{2\pi} \approx 5.3$ GHz and Q2 is tuned into resonance. The qubits are driven through one drive line, which is possible since there is cross coupling between the drive lines of the qubits and it is therefore possible to probe both qubits simultaneously. From the avoided crossing $\frac{2g_q}{2\pi} \approx 20$ MHz can be extracted from the energy splitting on resonance at this particular frequency. Of course coupling qubits to each other is done with the purpose of eventually applying computational gates. In this experiment it was sought to entangle the two qubits in order to implement full state tomography in a similar way as in Ref. [28]. The entangling gate used is based on the so called swap oscillations discussed in Section 2.2. An example of a swap measurement is shown in Fig. 4.13(b). Q2 is prepared in $|1\rangle$ with an X pulse with the two qubits detuned ~ 200 MHz from each other such that the qubits are decoupled. By applying a DC square pulse of varying width, τ, and amplitude, ΔV_2, the qubits are brought into or near resonance with each other. At resonance the qubit excitation oscillates between the two qubits. The frequency of the swap oscillations is given by, $\sqrt{(2g_q)^2 + \delta_q^2}\Big/2\pi$, where $\delta_q = \omega_{01}^{(1)} - \omega_{01}^{(2)}$ [29]. Therefore the point of slowest oscillation will correspond to $\delta_q = 0$ providing a direct measure of g_q, which in Fig. 4.13(b) corresponds to $\Delta V_2 = 27.9$ mV. By fitting a decaying sinusoid, $A\sin(2g_q t + \phi)\exp(-t/T) + b$, to the swap oscillations measured for both qubits at this point, the frequency of the swap oscillations is extracted to be $2g_q/2\pi = 23.0 \pm 0.1$ MHz at this particular point in the spectrum. The linecut at $\Delta V_2 = 27.9$ mV is shown in Fig. 4.14, where it should be noted that the oscillations are π out of phase consistent with swapping of the single photon excitation between the two qubits.

An iSWAP gate brings the qubit states from $|01\rangle$ to $|10\rangle$ and can therefore be calibrated from the swap oscillations. In Fig. 4.13(d) $\tau = 24$ ns and $\Delta V_2 = 27.9$ mV correspond to a full swap. A $\sqrt{\text{iSWAP}}$ gate is defined as the gate that brings the two states into equal superposition, in this case this occurs for $\tau = 12$ ns and $\Delta V_2 = 27.9$ mV.

4.7 Tomography

From the swap oscillations it is clear that coherent entanglement of the two qubits is possible. With the new single shot readout tomography measurements mapping out the full density matrix of the two-qubit system can potentially be carried out. Tomography can be understood as measurements of the state vector of a quantum system. This is done by preparing the same qubit state for repetitive measurements where the different components of the the vector are measured. X and Y measurements are performed by projecting onto the z-axis with a Y/2 or X/2 pulse. To map out the 2×2 density matrix of a single qubit state three measurements are needed, one each for the x-,y- and z-components. The fourth matrix element is given by normalisation. To proceed to

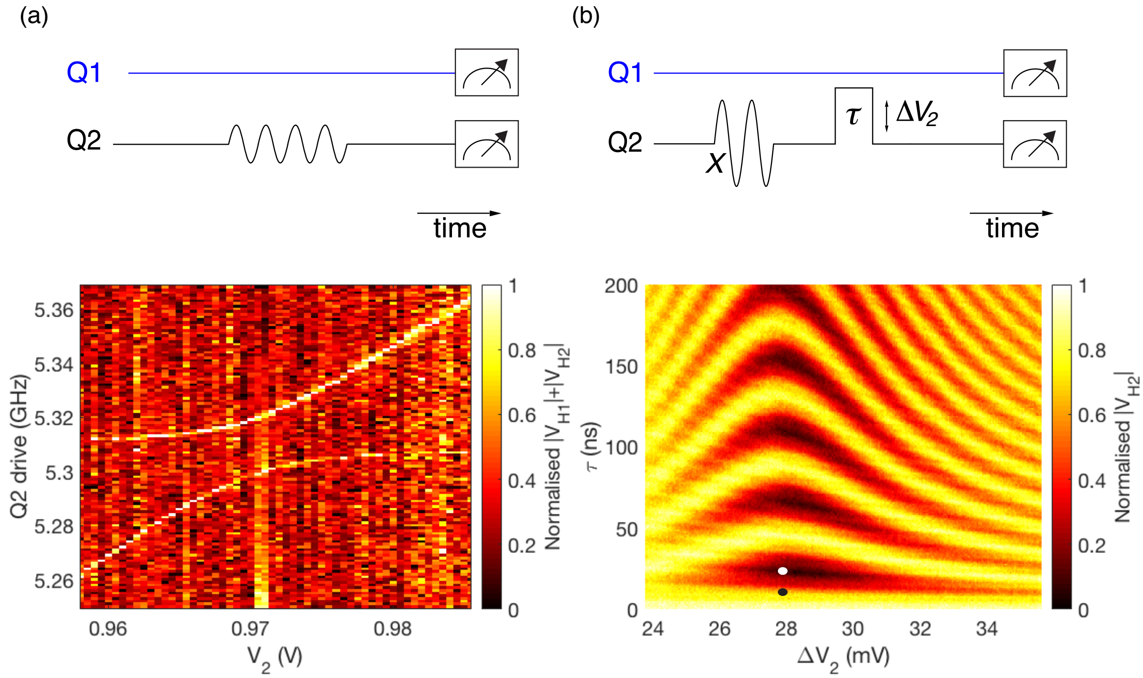

Figure 4.13: (a) Pulse scheme and two qubit spectroscopy measurement probing the avoided level crossing of Q1 and Q2. Both qubits are driven through Q2 with a broad -60 dBm microwave pulse, which creates some excited state population when on resonance. Both qubits are read out after the qubit drive pulse. The colour scale shows the normalised sum of the heterodyne readout response, $|V_{H1}| + |V_{H2}|$. From the avoided crossing $\frac{2g}{2\pi} \approx 20$ MHz. (b) Swap measurement data and pulse scheme. Q2 is prepared in $|1\rangle$ with an X pulse (a π pulse around the X-axis) and Q1 is left in $|0\rangle$. Q1 and Q2 are brought into resonance with each other by applying a gate pulse of varying amplitude, ΔV_2, and width, τ. The colour scale shows the normalised transmitted signal $|V_{H2}|$. A similar graph is recorded for Q1, where excitation probability is reversed compared to Q2. The white (black) dot indicates the value of τ and ΔV_2 that correspond to a $\sqrt{\text{iSWAP}}$ (iSWAP) gate.

measure the 4×4 two qubit density matrix it is needed to measure the 9 different combinations of X, Y and Z measurements in the simplest scheme [28]. This is because of the ability of measuring single qubit states independently. Other readout schemes, where the joint state is read out, 15 measurements are needed.

The simplest possible tomography experiment is measuring the single qubit density matrix of a qubit prepared in $|0\rangle$. These measurements are done by repeating X, Y and Z measurements 10^4 times and for every single measurement point the qubit state is determined with a threshold. If the qubit is measured in $|0\rangle$ the point is assigned with a -1 and if $|1\rangle$ is detected the point is assigned with 1. The mean value of these detection measurements corresponds to an expectation value of the Pauli operators, $\hat{\sigma}_x$, $\hat{\sigma}_y$, $\hat{\sigma}_z$, as shown in Fig. 4.15 (b). The qubit state is determined following the same procedure as in Fig. 4.9. The histograms created from the IQ-measurements are shown for the X measurement in Fig. 4.15 (a). Similar histograms are created for the Y and Z measurement.

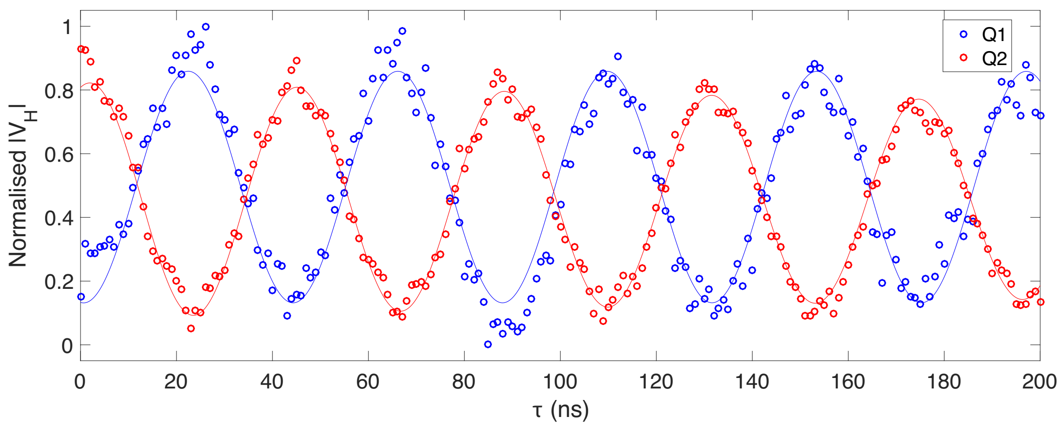

Figure 4.14: Linecut of the swap oscillations at $\Delta V_2 = 27.9$ mV. By fitting $A\sin(2g_q t + \phi)\exp(-t/T) + b$ to both qubits $2g_q/2\pi = 23.0 \pm 0.1$ MHz is extracted.

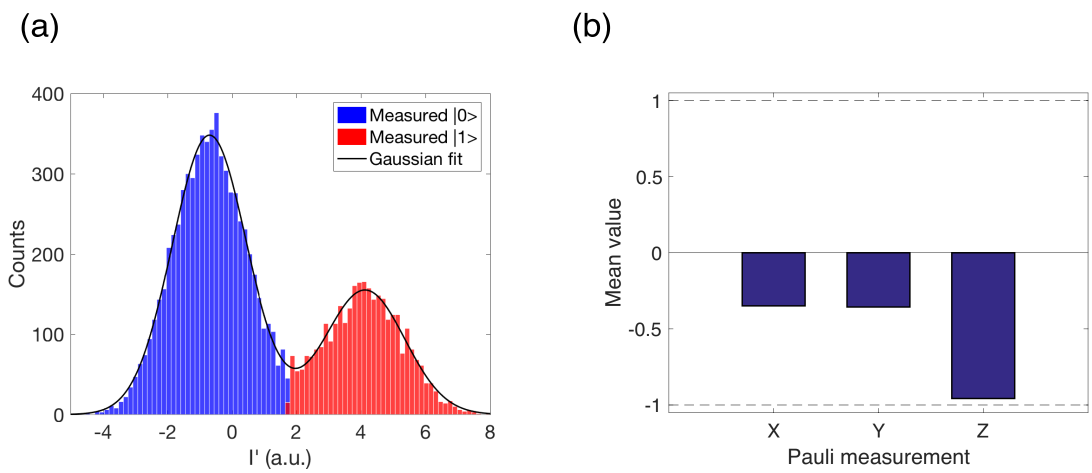

Figure 4.15: Simple single qubit tomography measurement. (a) Histogram of projected IQ-data onto the line providing highest separation. By fitting a sum of two Gaussians a threshold is set to determine whether a measurement is in $|0\rangle$ or in $|1\rangle$. The histogram shows the data from an X measurement. Similar histograms are generated for the Y and Z measurements. (b) Average measured value of the three Pauli matrices for a single qubit prepared in $|0\rangle$. Each point is generated from 10^4 measurements, where each point is assigned with a -1 if the qubit is in $|0\rangle$ or 1 if the qubit is in $|1\rangle$.

As the qubit is prepared in $|0\rangle$ it is expected to find $\langle\hat{\sigma}_x\rangle = \langle\hat{\sigma}_y\rangle = 0$ and $\langle\hat{\sigma}_z\rangle = -1$ in a perfect experiment. It is observed that $\langle\hat{\sigma}_x\rangle \approx \langle\hat{\sigma}_z\rangle \approx -0.35$, as expected due to decay. The Z measurement yields $\langle\hat{\sigma}_z\rangle \approx -0.95$, which is most likely due to some thermal equilibrium population of $|1\rangle$.

To investigate two qubit tomography the qubits are first prepared with a $\sqrt{\text{iSWAP}}$ gate calibrated from swap oscillations. Hereafter the nine different combinations of X, Y and Z measurements are performed using the pulse scheme shown in Fig. 4.16(a). The results of this measurement are shown in Fig. 4.16(b). Further, a tomography measurement after a iSWAP gate is performed, as shown in Fig. 4.16(c). In both Fig. 4.16(b) and 4.16(c) the expected results for an ideal system are shown. Since the iSWAP gate prepares the $|10\rangle$ state, which is not an entangled state no correlations are expected to be found. However for each measurement it is expected to measure -1 on Q1 and 1 on Q2, which leads to the expected values $\langle ZZ\rangle = \langle IZ\rangle = -1$ and $\langle ZI\rangle = 1$. The $\sqrt{\text{iSWAP}}$ gate on the other hand prepares an entangled state, $|\psi\rangle = \frac{1}{\sqrt{2}}(|01\rangle + i\,|10\rangle)$ [30]. The expected correlation values are constructed by evaluating,

$$\langle\hat{\sigma}_i\hat{\sigma}_j\rangle = \langle\psi|\,\hat{\sigma}_i \otimes \hat{\sigma}_j\,|\psi\rangle\,, \tag{4.5}$$

where ij can take the 9 combinations of x, y and z.

With the huge decay error in these measurements the results are not expected to reach the near the ideal values. In particular when measuring correlations the measurements are susceptible to decay errors on both qubits. This means that with ≈ 40 % error on Q1 and $\approx 30\%$ error on Q2 there is $\sim 40\%$ chance of measuring both qubits correctly. Regardless of the poor measurement fidelity, the results suggest that something else went wrong in the experiment. An indication of this, for instance, is that Q1 shows almost the same result in both cases. Since this device showed poor coherence times it was decided to proceed with other experiments rather than trying to optimise tomography on this device. I speculate that the randomness in the results may have been caused by qubit drift between calibrating the gates from the swap oscillations and the actual measurement. As seen from Fig. 4.13(b) a drift in the qubit frequency of either qubit will lead to faster oscillations if the detuning of the qubits is close enough that the coupling is still sufficient. The iSWAP and $\sqrt{\text{iSWAP}}$ then become random uncontrolled gates instead. However I believe that with the present setup future prospects of measuring entanglement are promising if the challenge of prolonging gatemon lifetimes can be overcome.

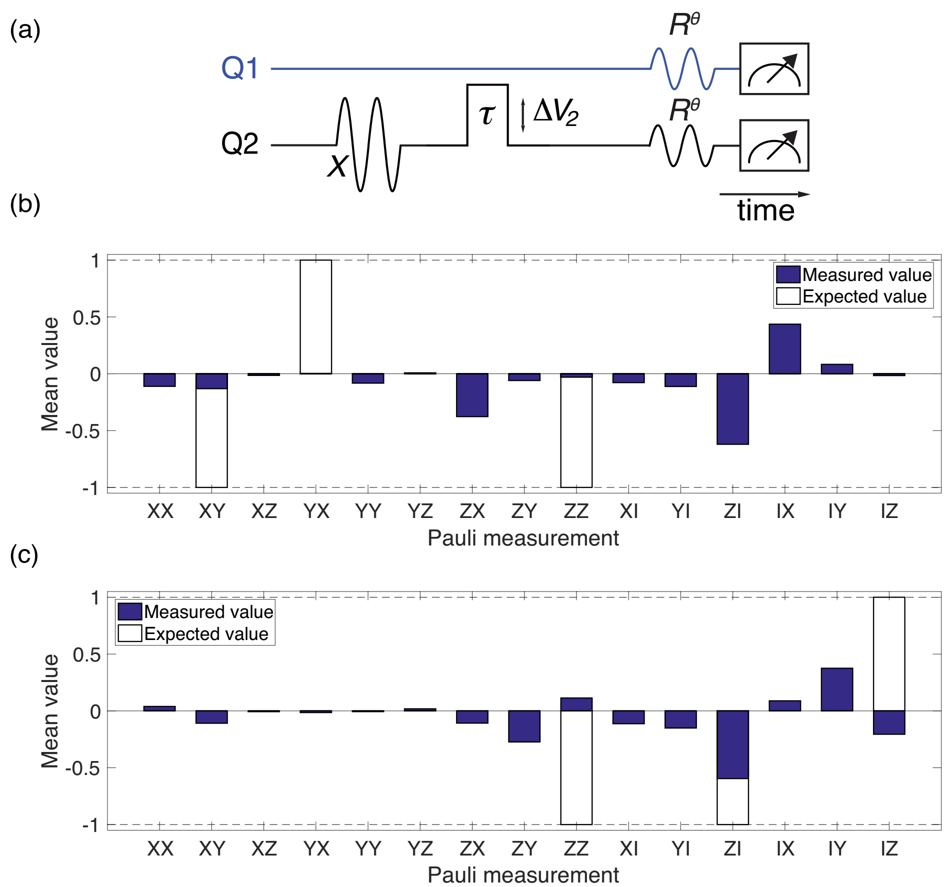

Figure 4.16: (a) Pulse scheme for measuring the two qubit density matrix. The first part is the same as used to perform swap oscillations. Here specific values of τ and ΔV_2 are chosen to perform a $\sqrt{\text{iSWAP}}$ in (b) and an iSWAP gate in (c). To construct all nine combinations of X, Y and Z measurements the qubits are either projected to the z-axis with an X/2 pulse to do a Y measurement or Y/2 pulse to an X measurement or no pulse is applied to do a Z measurement. These three combinations for each qubits are represented by R^θ in the figure. (b) Average values for the Pauli measurements with the qubits prepared in an entangled state with a $\sqrt{\text{iSWAP}}$ gate. The first nine data points are the product combinations of the Pauli measurements of the two qubits. The IJ label on the x-axis indicates which coordinate is measured with the first label being on Q1 and the second being on Q2. The last six points are the average values of the single qubit Pauli measurements, where I refers to no measurement on the qubit. The blue bars show the actual measured values and the white bars show the expected ideal outcome. (c) Same as (b) except the qubits are prepared with an iSWAP gate instead.

Chapter 5

Conclusions and outlook

In this thesis a two-qubit nanowire based semiconductor/superconductor qubit device has been successfully fabricated using conventional lithography techniques. This device was shown to be controllable over the entire qubit space with microwave pulses and gate voltage pulses and the characteristic coherence times of the system were measured to be $\sim$ 1-2 µs. Measurements of this device investigated the implementation of several new techniques.

The integration of a new travelling parametric amplifier into the existing cryogenic setup was examined with the purpose of achieving high fidelity qubit state determination. Measurements carried out on this qubit device have shown that prepared $|0\rangle$ and $|1\rangle$ states can be read out with 70% fidelity. Further analysis showed that qubit decay is by far the dominant contributor to the readout error, with $T_1 = 1.6$ µs. Therefore future prospects of achieving high fidelity readout relies on coherence to improve in future gatemon experiments. As conventional transmon devices consistently show lifetimes a factor of 10-20 higher than gatemon devices, larger coherence is believed to be achievable.

In this thesis it was also examined whether full qubit control can be achieved using only one on-chip line. This experiment was performed by loading two identically designed and fabricated qubits with different wiring. Single line control required DC and microwave signals be effectively combined by integrating new bias-tees into the setup. A filtering configuration that minimises thermal noise and at the same time allows microwave frequencies in the range $\sim$ 3-7 GHz to pass through is also required. To test if single line control degrades qubit coherence the performance of the two qubits was characterised where one qubit was a reference qubit and one qubit was single line controlled. Both qubits showed coherence times of the same order of magnitude, but the coherence of the single line controlled qubit seems consistently shorter. It is unclear whether this is due to variations in fabrication and therefore further investigation is proposed. Before implementing single line control for all future gatemon designs, new devices need to demonstrate longer coherence times and it then needs to be shown that they are not degraded by the single line control.

The last main result of this thesis work was the implementation of simple feedback procedures. This is very interesting because gatemons show unique non-monotonic frequency spectra with steep regions very susceptible to frequency drift and more stable sweet spots. Building a multiple qubit device that relies on sweet spot operation is hard to imagine and therefore frequency feedback is required. This first attempt to correct frequency is based on tracking the qubit frequency with Ramsey measurements and the correcting the drift by stepping the gate voltage accordingly. These measurements clearly showed that it is possible to correct frequency drift potentially allowing stable gatemon operations in steep frequency regions. Having demonstrated basic operation, it will be very desirable for future experiments to incorporate faster feedback schemes into gatemon algorithms.

It is clear that a systematic study on improving gatemon coherence times is needed before the unique advantages of the gatemon make it an attractive qubit. With that said the demonstrations of single line control, feedback and single shot readout are promising steps towards building a competitive qubit system with gatemons.

Appendix A

Fabrication

The gatemon qubit devices are fabricated using standard lithography techniques. Bellow follows a detailed recipe used for the two-qubit device. This recipe will generally apply to fabricating other gatemon devices.

AL film

- Load Si wafer into AJA International metal evaporation system
- Evaporate 100 nm of Al on a Si argon milled wafer

Lines, qubits islands, resonator etch

- Spin AZ1505 photo resist at 4000 rpm for 45 s and bake the resist at 115°C for 1 min
- Expose design with Heidelberg LED blaster, expose each write field 30 ms, defocus -5
- Develop the resist with AZ developer for 40 s followed by 30 sMilli-Q water and 4 min plasma ash.
- Etch out the pattern with 1 min Transcene Al etchant type D followed by 10+30 s Milli-Q water rinse.

LED defined marks

- Spin AZ1505 photo resist at 4000 rpm for 45 s and bake the resist at 115°C for 1 min
- Expose design with Heidelberg LED blaster, expose each write field 30 ms, defocus -5
- Develop the resist with AZ developer for 40 s followed by 30 sMilli-Q water and 4 min plasma ash
- Evaporate 5 nm Ti followed by 80 nm Au
- Lift off 80°C NMP for 1h followed by 30 s sonication. Rinsed in acetone, IPA and 4 min Ash

Wire alignments marks

- Spin EL9/csar9 EBL resist at 4000 rpm for 45 s and bake resist 1+3 min 185°C
- Define pattern with Elionix ELS- 7000 EBL system with a dose time of 0.56 µs, beam current: 2 nA, write field size: 300 µm, 20000 dots
- Over night lift off in acetone 2 min sonication in IPA+2 min Ash

Wire windows

- Spin EL9 EBL resist at 4000 rpm for 45 s and bake resist 3 min 185°C
- Define pattern with Elionix EBL system with a dose time of 0.26 µs, beam current: 5 nA, write field size: 300 µm, 20000 dots

Cleaving

- Cleaved chip in 9 pairs using Loomis automatic scriber with a scribe pressure of 1.8 psi and break pressure of 6.0 psi

Wire placement

- develop 75 s 1:3 MIBK:IPA followed by 10 s IPA rinse and 1 min Ash
- Randomly place nanowires in the defined windows with the tip of a cleanroom wipe
- Strip resist by rinsing chip in acetone, IPA and 2 min Ash

Wire junction etch

- Spin PMMA 4% EBL resist at 4000 rpm for 45 s and bake resist 3 min 185°C
- Load optical Images into design file for alignment of design to nanowires
- Define etch windows with EBL, dose time: 0.3 µs, area dose: 1200 $\frac{\mu C}{cm^2}$ beam current: 1 nA, write field size: 300 µm, 60000 dots
- develop 60 s 1:3 MIBK:IPA followed by 10 s IPA rinse and 1 min Ash
- Etch nanowire junction with 1 min Transcene Al etchant type D followed by 30 s Milli-Q water, 10 s IPA rinse and nitrogen blow dry
- Strip resist by rinsing chip in acetone, IPA and 2 min Ash
- SEM image the etched nanowires to find suitable candidates for the qubit junction

Contacts and sidegate

- Spin El9+PMMA 4% EBL resist at 4000 rpm for 45 s and bake resist 1+3 min 185°C
- load SEM images to design for gates+contacts,
- Define gate and contact pattern with EBL, dose time: 0.3 μs, area dose: 1200 $\frac{\mu C}{cm^2}$ beam current: 1 nA, write field size: 300 μm, 60000 dots
- develop 60 s 1:3 MIBK:IPA followed by 10 s IPA rinse and 1 min Ash
- Load sample into AJA evaporation system, argon mill oxide layer on nanowire for 4.5 min, evaporate 1 nm Ti and 1 nm Al
- Lift off 80°C NMP for 1h followed by 30 s sonication. Rinsed in acetone, IPA and 2 min Ash

Wire Bonding

- Glued to PCB sample board with PMMA
- Al wire bonded control lines to PCB sample board
- Loading in indium sealed Al box and puck

Appendix B

Transport measurements

The first gatemon devices were fabricated with a InAs core epitaxially macthed with a full Al shell (named QDev 70). As these devices showed some undesired features as non-monotonic IV-characteristic, low gateability and low stability a test of various nanowires and gating schemes was conducted as part of my thesis work. In Fig. B.1 an example of a 4 probe current bias measurement on a top gated QDev70 device. Along with this data set is a list summarising the results of these measurements. All measurements are carried out by sweeping gate voltage on the junction and the current sent through the nanowire. By measuring the voltage across the junction allows the resistance to be extracted.

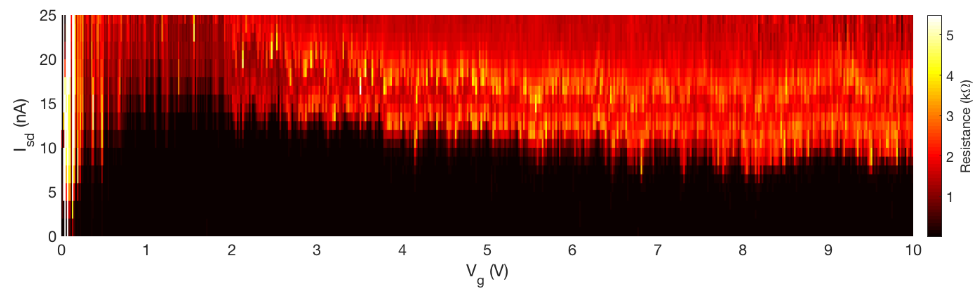

Figure B.1: Resistance data of a 4-probe measurement across a nanowire junction. The gate voltage, V_g, and the current, I_{sd}, across the nanowire are varied. A region of zero resistance is clearly observed reached. For a given V_g I_c can be extracted as the value of I_{sd}, where there is a transition from no resistance to a large resistance. For the this device the maximum value of $I_c \approx 15$ nA.

Bottom gated test devices

Qdev 70

- Wire type: 80 nm InAs core, 25-30 nm Al shell - hexagonal cross section
- Junction length: 150 and 200 nm

- Room temperature resistance across junction: 12 and 34 kΩ
- Measured I_c: No detected supercurrent, measured short to ground in one device and no contact in the other.
- Device: 20 nm high and 200 nm Al bottom gates covered with a 5 nm HfO dielectric with the nanowire suspended on 50 nm Al pads.

Qdev 96

- Wire type: 200 nm InAs core, 10-20 nm Al shell - hexagonal cross section
- Junction length: 150 and 200 nm
- Room temperature resistance across junction: 12 and 34 kΩ
- Measured I_c: 1-5 nA, completely pinch off at negative voltages, 10 V range to open completely. $R \approx 5\text{k}\Omega$ above I_c
- Device: 20 nm high and 200 nm Al bottom gates covered with a 5 nm HfO dielectric with the nanowire suspended on 50 nm Al pads.

Qdev 152

- Wire type: 100 nm InAs core, 25-30 nm Al shell - circular cross section
- Junction length: 150 and 200 nm
- Room temperature resistance across junction: 12 and 34 kΩ
- Measured I_c: No detected supercurrent, either no contact or very high resistance across junction
- Device: 20 nm high and 200 nm Al bottom gates covered with a 5 nm HfO dielectric with the nanowire suspended on 50 nm Al pads.

Qdev 225

- Wire type: 100 nm InAs core, < 10 nm GaAs , 25-30 nm Al shell - hexagonal cross section
- Junction length: 200 nm
- Measured I_c: 10-20 nA, completely pinch off at negative voltages, 10 V range to open completely. $R \approx 5\text{k}\Omega$ above I_c
- Device: 20 nm high and 200 nm Al bottom gates covered with a 5 nm HfO dielectric with the nanowire suspended on 50 nm Al pads.

Qdev 269

- Wire type: 40-50 nm InAs core, 5 nm GaAs , 25-30 nm Al shell - hexagonal cross section
- Junction length: 130-200 nm
- Measured I_c: No super current observed and no gateability of the junctions.
- Room temperature resistance: few kΩto tens of kΩ
- Device: 20 nm high and 200 nm Al bottom gates covered with a 5 nm HfO dielectric with the nanowire suspended on 50 nm Al pads.

Top gated test devices

Qdev 70

- Wire type: 80 nm InAs core, 25-30 nm Al shell - hexagonal cross section
- Junction length: 150 and 200 nm
- Room temperature resistance across junction: 12 and 34 kΩ
- Measured I_c: < 15 nA, very high gateability and smooth pinch off.
- Room temperature resistance: few kΩ to hundreds of kΩ.
- Device: 150 nm high and 200 nm wide Al topgates separated from the nanowire with a 15 nm ZrO_2 annealed dielectric following a recipe from [31].

Side gated test devices

- Wire type: 80 nm InAs core, 25-30 nm Al shell - hexagonal cross section
- Junction length: 150 and 200 nm
- Room temperature resistance across junction: 2 kΩ on both wires
- Measured I_c: 80 nA , ~ 10 V to open junction completely and difficult to pinch of.
- Device: 150 nm high and 200 nm wide Al sidegates deposited 100 nm from the nanowire junction.

Conclusions

As most of the wires showed either low or no I_c none of the alternative wires have been implemented in qubit devices. The most promising lesson from the measurements is the strong and smooth gateability of the topgate. Because the device showed $I_c < 15$nA, which correspond to a maximum qubit frequency of:

$$E_J = \frac{\hbar I_c}{2e}, f_{01} = \frac{E_{01}}{2e} \approx \frac{\sqrt{8E_C E_J}}{h} \approx 3.5 \text{ GHz}$$

a topgated qubit device was not pursued. However this strong gateability is promising for using topgated tuneable couplers, which have been investigated in other gatemon experiments.

Bibliography

[1] B. M. Terhal. Quantum error correction for quantum memories. *Reviews of Modern Physics*, 87(2), 2015.

[2] M. Reiher, N. Wiebe, K. M. Svore, D. Wecker, and M. Troyer. Elucidating reaction mechanisms on quantum computers. *arXiv preprint arXiv:1605.03590*, 2016.

[3] D. P. DiVincenzo. The physical implementation of quantum computation. *arXiv preprint quant-ph/0002077*, 2000.

[4] C. Monroe and J. Kim. Scaling the ion trap quantum processor. *Science*, 339(6124), 2013.

[5] R. Hanson, L. P. Kouwenhoven, J. R. Petta, S. Tarucha, and L. M. K. Vandersypen. Spins in few-electron quantum dots. *Reviews of Modern Physics*, 79(4):1217–1265, 2007.

[6] C. W. J. Beenakker. Search for majorana fermions in superconductors. *arXiv preprint arXiv:1112.1950*, 2011.

[7] J. Kelly, R. Barends, A. G. Fowler, A. Megrant, E. Jeffrey, T. C. White, D. Sank, J. Y. Mutus, B. Campbell, Yu. Chen, Z. Chen, B. Chiaro, A. Dunsworth, I. C. Hoi, C. Neill, P. J. J. O'Malley, C. Quintana, P. Roushan, A. Vainsencher, J. Wenner, A N. Cleland, and J. M. Martinis. State preservation by repetitive error detection in a superconducting quantum circuit. *Nature*, 519(7541), 2015.

[8] S. Sheldon, E. Magesan, J. M. Chow, and J. M. Gambetta. Procedure for systematically tuning up cross-talk in the cross-resonance gate. *Phys. Rev. A*, 93:060302, 2016.

[9] T. W. Larsen, K. D. Petersson, F. Kuemmeth, T. S. Jespersen, P. Krogstrup, J. Nygård, and C. M. Marcus. Semiconductor-Nanowire-Based Superconducting Qubit. *Physical Review Letters*, 115(12):127001, 2015.

[10] G. de Lange, B. van Heck, A. Bruno, D. J. van Woerkom, A. Geresdi, S. R. Plissard, E. P. A. M. Bakkers, A. R. Akhmerov, and L. DiCarlo. Realization of Microwave Quantum Circuits Using Hybrid Superconducting-Semiconducting Nanowire Josephson Elements. *Physical Review Letters*, 115:127002, 2015.

[11] L. Casparis, T. W. Larsen, M. S. Olsen, F. Kuemmeth, P. Krogstrup, J. Nygård, K. D. Petersson, and C. M. Marcus. Gatemon Benchmarking and Two-Qubit Operations. *Physical Review Letters*, 116(15):150505, 2016.

[12] S. M. Girvin. Circuit QED: Superconducting Qubits Coupled to Microwave Photons. 2015.

[13] M. Tinkham. *Introduction to superconductivity.* Courier Corporation, 1996.

[14] M. H. Devoret, A. Wallraff, and J. M. Martinis. Superconducting Qubits: A Short Review . *arXiv preprint cond-mat/0411174*, 2004.

[15] J. Koch, T. M. Yu, J. Gambetta, A. A. Houck, D. I. Schuster, J. Majer, A. Blais, M. H. Devoret, S. M. Girvin, and R. J. Schoelkopf. Charge-insensitive qubit design derived from the Cooper pair box. *Physical Review A*, 76(4):042319, 2007.

[16] M. D. Reed. Ph.D. thesis, Entanglement and Quantum Error Correction with Superconducting Qubits. Yale University, 2013.

[17] A. Blais, R. S. Huang, A. Wallraff, S. M. Girvin, and R. J Schoelkopf. Cavity quantum electrodynamics for superconducting electrical circuits: An architecture for quantum computation. *Physical Review A*, 69(6):062320, 2004.

[18] D. I. Schuster. Ph.D. thesis, Circuit Quantum Electrodynamics. Yale University, 2008.

[19] A. A. Houck, J. A. Schreier, B. R. Johnson, J. M. Chow, J. Koch, J. M. Gambetta, D. I. Schuster, L. Frunzio, M. H. Devoret, S. M. Girvin, and R. J. Schoelkopf. Controlling the Spontaneous Emission of a Superconducting Transmon Qubit. *Physical Review Letters*, 101(8):080502, 2008.

[20] L. M. K. Vandersypen and I. L. Chuang. Nmr techniques for quantum control and computation. *Reviews of modern physics*, 76(4):1037, 2005.

[21] A. Dewes, F. R. Ong, V. Schmitt, R. Lauro, N. Boulant, P. Bertet, D. Vion, and D Esteve. Characterization of a two-transmon processor with individual single-shot qubit readout. *Physical review letters*, 108(5):057002, 2012.

[22] P. Krogstrup, N. L. B. Ziino, W. Chang, S. M. Albrecht, M H. Madsen, E. Johnson, J. Nygård, C. M. Marcus, and T. S. Jespersen. Epitaxy of semiconductor–superconductor nanowires. *Nature Materials*, 14(4), 2015.

[23] T. Ihn. *Semiconductor Nanostructures: Quantum states. and electronic transport.* Oxford University Press, 2010.

[24] C. Macklin, K. O'Brien, D. Hover, M. E. Schwartz, V. Bolkhovsky, X. Zhang, W. D. Oliver, and I. Siddiqi. A near–quantum-limited josephson traveling-wave parametric amplifier. *Science*, 350(6258), 2015.

[25] K. O'Brien, C. Macklin, I. Siddiqi, and X Zhang. Resonant Phase Matching of Josephson Junction Traveling Wave Parametric Amplifiers. *Physical Review Letters*, 113(15):157001, 2014.

[26] E. Jeffrey, D. Sank, J. Y. Mutus, T. C. White, J. Kelly, R. Barends, Y. Chen, Z. Chen, B. Chiaro, A. Dunsworth, A. Megrant, P. J. J. O'Malley, C. Neill, P. Roushan, A. Vainsencher, J. Wenner, A. N. Cleland, and J. M. Martinis. Fast Accurate State Measurement with Superconducting Qubits. *Physical Review Letters*, 112(19):190504, 2014.

[27] R. J. Barlow. *Statistics: a guide to the use of statistical methods in the physical sciences*, volume 29. John Wiley & Sons, 1989.

[28] J. Cramer. Master's thesis, Algorithmic speedup and multiplexed readout in scalable circuit. Delft University of Technology, 2012.

[29] M. Hofheinz, H. Wang, M. Ansmann, R. C. Bialczak, E. Lucero, M. Neeley, A. D. O'Connell, D. Sank, J. Wenner, J. M. Martinis, and A. N. Cleland. Synthesizing arbitrary quantum states in a superconducting resonator. *Nature*, 459(7246), 2009.

[30] J. M. Chow. Ph.D. thesis, Quantum Information Processing with Superconducting Qubits. Yale University, 2010.

[31] S. Chuang, Q. Gao, R. Kapadia, A. C. Ford, J. Guo, and A. Javey. Ballistic InAs nanowire transistors. *Nano letters*, 13(2), 2013.